https://doi.org/10.5194/wes-2026-99
Preprint. Discussion started: 15 July 2026

eawe european academy of wind energy
Open Access WIND ENERGY SCIENCE DISCUSSIONS

Beyond the Intersection Point: Offshore Wind and Turbulence Reconstruction from Horizontally Separated Dual-Doppler Scanning Lidar Beams

Farkhondeh (Hanie) Rouholahnejad[1,2], Tanguy Lunel[3,4], and Julia Gottschall[1,2]

[1]Fraunhofer Institute for Wind Energy Systems IWES, Am Seedeich 45, 27572 Bremerhaven, Germany
[2]Faculty of Geosciences, University of Bremen, Klagenfurter Str. 4, 28359 Bremen, Germany
[3]Centre National de Recherches Météorologiques, Météo-France, CNRS, Université de Toulouse, Toulouse, France
[4]France Énergies Marines, Technopole Brest-Iroise, 525 Avenue Alexis de Rochon, Plouzané 29280, France

Correspondence: Farkhondeh (Hanie) Rouholahnejad (farkhondeh.rouholahnejad@iwes.fraunhofer.de)

Abstract. Dual-Doppler scanning lidars (DSLs) are increasingly considered a promising technology for offshore turbulence characterization, yet their performance at long offshore ranges and their sensitivity to spatial separation between reconstructed measurement volumes remain largely unexplored. Conventional DSL configurations require the two lidar beams to intersect at a common measurement volume, whereas many other single-lidar-based wind retrieval techniques rely on assumptions of horizontal flow homogeneity to combine measurements obtained at different locations. This study investigates whether the requirement for intersecting range gates can be relaxed in offshore environments and whether non-collocated dual-Doppler reconstructions can provide useful information on spatial variability. A four-month offshore measurement campaign was conducted near Blyth, UK, using three scanning lidars and an offshore meteorological mast. Collocated DSL reconstructions at ranges of 5–7 km were first validated against cup-anemometer to establish a baseline uncertainty. Subsequently, synchronized range gates with horizontal separations of 500, 1000, and 1500 m were used to quantify the impact of non-collocation on reconstructed wind statistics. The observed deviations were further analyzed using a large-eddy simulation case study. The collocated configuration provided accurate wind speed estimates and TI biases within ± 0.01. For wind speeds up to 9 ms^{-1}, non-collocated reconstructions with separations up to 500 m produced uncertainties comparable to the baseline TI measurement uncertainty. Larger separations resulted in increasing deviations, particularly in heterogeneous flow conditions influenced by coastal transitions and wind turbines. Comparison with LES demonstrated that these deviations reflect physically meaningful spatial variability rather than measurement artifacts. The results indicate that strict range-gate intersection is not always required for offshore dual-Doppler reconstruction. Under sufficiently homogeneous offshore conditions, moderate beam separations can be tolerated, while the resulting deviations provide a practical measure of spatial uncertainty relevant for wind resource assessment and load analysis.

1 Introduction

The financial viability and bankability of offshore wind projects depend on accurate wind resource assessments, including reliable estimates of mean wind speed, wind direction, and ambient turbulence intensity (TI). Remote-sensing solutions are

https://doi.org/10.5194/wes-2026-99
Preprint. Discussion started: 15 July 2026

generally preferred over in-situ measurements offshore due to their flexibility and cost-effectiveness. Doppler wind lidars have become an established tool for offshore wind resource assessment and have demonstrated high accuracy in measuring mean wind speed and wind direction when compared with conventional meteorological references.

Turbulence is considerably more challenging to characterize with lidar measurements than mean flow statistics (Sathe et al., 2011). The representation of turbulent fluctuations depends on the beam orientation relative to the mean wind direction (Peña and Mann, 2019) and on atmospheric conditions, particularly the turbulence length scale, due to attenuation resulting from probe-volume averaging (Kaimal and Finnigan, 1994; Frehlich, 1997; Mann et al., 2009). Furthermore, variations in atmospheric aerosol concentration can affect signal quality, introducing measurement noise and data gaps that may distort turbulence statistics. Additional uncertainties arise from the measurement configuration and deployment conditions. For example, platform motion can contaminate turbulence measurements if not adequately corrected for Floating Lidar Systems (Gottschall et al., 2017; Watson et al., 2025).

Among currently available offshore remote-sensing technologies, dual-Doppler scanning lidars (DSLs) are considered one of the most promising approaches for TI characterization. Their capabilities has been demonstrated in several recent studies, and evidence supporting their application for offshore turbulence characterization continues to grow (Frehlich, 1997; Berg et al., 2015; Newsom et al., 2015; Pauscher et al., 2016; Carbon Trust, 202; Shimada et al., 2022, 2025).

Traditionally, dual-Doppler scanning lidar systems are operated such that the two lidar beams intersect at a common measurement volume (with a tolerance in the order of tens of meters), enabling the reconstruction of the horizontal wind vector without assumptions regarding flow direction other than the neglect of the vertical wind component projected onto the line-of-sight (LOS). Using lidar simulations, Cheynet et al. (2017) quantified the attenuation of wind variance due to probe-volume averaging and reported an underestimation of approximately 20% for a probe length of 100 m. Peña and Mann (2019) investigated the same effect using a pair of WindCube 200S scanning lidars observing a sonic anemometer from distances between 1 and 1.6 km and reported a 15% underestimation of the reconstructed variance together with an R^2 of 0.91. Using three Stream Line lidars, Fuertes et al. (2014) reconstructed the three-dimensional turbulence field and found good agreement with sonic measurements once the sonic data were filtered using a Gaussian spatial convolution to account for lidar attenuation. Similar conclusions were reported by Pauscher et al. (2016), who demonstrated improved agreement of LOS variance estimates after accounting for probe-volume averaging and showed that the scan configuration influences the accuracy and precision of the reconstructed variance.

Building upon these single-point turbulence studies, several authors have explored the use of scanning lidar systems for the retrieval of turbulence information at multiple heights. Newsom et al. (2015) demonstrated a virtual-tower dual-Doppler configuration and reported an underestimation of approximately 15% compared to sonic measurements at 60 m height over a one-month campaign. More recently, Shimada et al. (2022) validated first- and second-order statistics from a three-level offshore dual-Doppler configuration against cup anemometer measurements at 63 m height. Using a probe length of 50 m and reconstruction ranges of 1.6 and 2.5 km, the system achieved an R^2 of 0.86 for turbulence intensity.

While these studies demonstrate the capability of dual-Doppler scanning lidars to retrieve turbulence statistics, they were conducted at ranges of at most 2.6 km. Offshore wind-resource assessments often require higher ranges, for which larger

https://doi.org/10.5194/wes-2026-99
Preprint. Discussion started: 15 July 2026

probe lengths are necessary to maintain sufficient signal quality. The performance of dual-Doppler systems for turbulence characterization at these longer ranges therefore remains largely unexplored.

In addition, existing dual-Doppler applications have focused primarily on single-point measurements or virtual meteorological masts, providing local or vertical information. In contrast, spatial variations of mean wind speed and turbulence are commonly obtained from numerical models. The question therefore arises whether dual-Doppler scanning lidars can also provide information on the horizontal variability of turbulence statistics.

Another unexplored side of the DSL concept but well explored for profiling lidars or single lidar configurations is the the role of horizontal homogeneity assumption. Vertical profiling and volumetric scanning approaches exploit the assumption of horizontal flow homogeneity to combine measurements obtained at different locations and times for the reconstruction of wind speed and TI (Gottschall et al., 2012; Kelberlau and Mann, 2020; Peña and Mann, 2019; Newman et al., 2016). In contrast, dual-Doppler configurations directly reconstruct the horizontal wind vector without any assumption on the flow homogeneity. Given the relatively homogeneous flow conditions often encountered offshore, it is therefore worthwhile to investigate whether the homogeneity assumption can be exploited within a dual-Doppler framework by relaxing the requirement for collocated measurement volumes.

Accordingly, this study combines a dedicated measurement campaign with large-eddy simulation data to address the following research questions:

- How accurately can dual-Doppler scanning lidars measure mean wind speed and turbulence intensity under representative offshore conditions at extended ranges of 5–7 km and what is the uncertainty?
- To what extent can the requirement for co-located dual-Doppler measurements be relaxed by leveraging the horizontal homogeneity of offshore flow, and how does the resulting uncertainty depend on atmospheric conditions?
- Can non-collocated dual-Doppler scanning lidar measurements be used to quantify spatial variability in the wind field, and how do the resulting estimates compare with those obtained from large-eddy simulations?

The remainder of this paper is organized as follows. Firstly Section 2.1 describes the measurement campaign. Then, the dual-Doppler collocated and non-collocated reconstruction methodology are elaborated in Section 2.2. After presenting the atmospheric stability calculation and climatology during the campaign in Sections 2.3 and 2.4, the large-eddy simulation setup and validation is introduced in Section 2.5, followed by the validation concepts and error metrics in Section 2.6. The performance of collocated dual-Doppler scanning lidars for turbulence intensity measurements at long offshore ranges is evaluated in Section 3.1. The impact of increasing spatial separation between synchronized range gates on wind speed and TI is then investigated as a function of beam separation distance in Section 3.2. The analysis is further extended to different wind direction sectors and atmospheric conditions. Finally, the variability captured by non-collocated reconstructions are compared with LES in Section 3.3. The performance of DSL TI is discussed in Section 4.1 while the deviations resulting from range-gate separation are discussed in Section 4.2 and put in the context of flow homogeneity in Section 4.3. These deviations are subsequently interpreted as a measure of spatial uncertainty in Section 4.4. The limitations of the study are discussed in Section 4.5 , and the main conclusions are presented in Section 5.

https://doi.org/10.5194/wes-2026-99
Preprint. Discussion started: 15 July 2026

2 Methodology

We designed a demonstration campaign to investigate the aforementioned research questions. In this section we present the measurement campaign and the developed scan strategy as well as the reconstruction methods. A short period of this campaign was additionally simulated using Large Eddy Simulations, which is introduced in this section. Lastly, the validation exercises and the metrics and parameters used in this study are presented.

2.1 Measurement campaign

The measurement campaign was part of the "New methods for turbulence measurements and models in offshore wind" or "NEMO" project and took place between 30-04-2025 and 20-08-2025 at the Center for the Testing of Environmental Science Technology (C-TEST). The C-TEST site, operated by Oldbaum Services Limited, is located off the North Sea coast near the city of Blyth, UK, and consists of two major onshore installations: a southern site at East Quay, where instruments are deployed on top of a container and powered by a generator, and a northern site at the Newbiggin-by-the-Sea Maritime Center rooftop. These sites are located in a distance of approximately 5.3 km and 6.8 km, respectively, from the National Offshore Anemometry Hub (NOAH) offshore meteorological mast (see Figure 1a). During the four-month course of the campaign, three horizontally scanning lidars, along with other atmospheric sensors, were deployed at the northern and southern sites and operated to measure wind and atmospheric parameters. In addition, a wave buoy was measuring the wave parameters in the vicinity of the meteorological mast.

2.1.1 NOAH meteorological mast

The offshore meteorological mast is located at 55°08'46.400" N, 1°25'15.000" W in a water depth of approximately 38 m. The data provision is coordinated by National Offshore Anemometry Hub. The lattice mast was instrumented in 2012 and has been operational since then. The highest cup anemometer is installed at 103 m above mean sea level, while the highest wind vane is located at 101 m. Both record 10-min averages based on 1 Hz data. Measurements at approximately 100 m height were used as a reference for wind speed and TI, and to estimate atmospheric stability.

2.1.2 Wave Buoy

As part of the National Network of Regional Coastal Monitoring Programmes (NNRCMP) of England, a coastal wave monitoring network has been developed and maintained around the English coastline. The buoy used in this study has been deployed in June 2013 at the position 55° 11.11' N, 001° 28.69' W. According to the maintenance records, the last scheduled maintenance took place in June 2025,i.e. during the NEMO campaign. The observational data have undergone full quality assurance and quality control procedures following the standards described in the Waves Quality Control Manual (Channel Coastal Observatory, 2024).

Sea Surface Temperature (SST) data used in this analysis to calculate the bulk Richardson Number were obtained directly from the buoy dataset provided through the NNRCMP realtime data portal (National Network of Regional Coastal Monitoring

https://doi.org/10.5194/wes-2026-99
Preprint. Discussion started: 15 July 2026

eawe european academy of wind energy
Open Access WIND ENERGY SCIENCE DISCUSSIONS

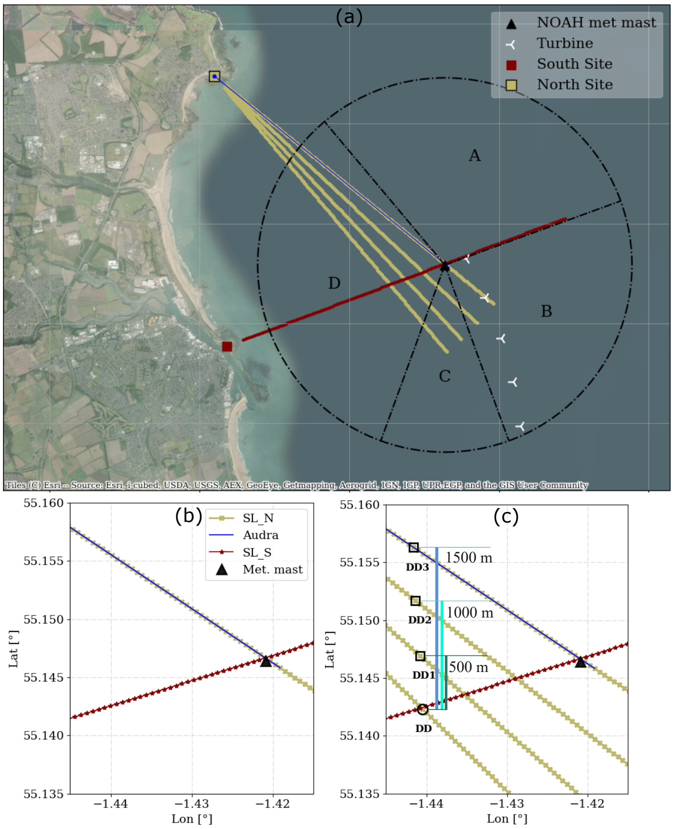

Figure 1. Panel (a) presents the relative positions of the South site, the North coastal site, and the NOAH meteorological mast. Sectors A–D indicate wind directions with distinct characteristics, which are analyzed in this study. Panels (b) and (c) depict the scan configurations for Phase 1 and Phase 2, respectively. During Phase 2, DD1–3 are positioned at the same height as DD. Basemap © Esri and its data partners | Powered by Esri.

Programmes, 2026). To ensure data reliability, only measurements that were not assigned quality-control flags 7 or 8 were retained for further analysis.

2.1.3 Scanning lidar systems

Three Vaisala WindCube Scan 400S systems were deployed at the C-TEST site for the purpose of the NEMO experiment and operated in two experimental phases. Two systems of the same generation (v2.1) were deployed at the northern (SL_N) and southern (SL_S) sites, while AUDRA which is from an earlier generation (v2.0) was deployed at the northern site. During the campaign the lidar pitch and roll were monitored daily by Oldbaum Services, and hard-target tests were performed as elaborated in Young et al. (2026), whenever deviations approached a chosen threshold of 0.05°.

Phase 1 was designed to quantify the baseline measurement capability, i.e., the baseline uncertainty of scanning lidars operated in a multi-point dual-Doppler configuration. For this purpose, all three scanning lidars were calibrated and configured

https://doi.org/10.5194/wes-2026-99
Preprint. Discussion started: 15 July 2026

such that their beams intersected at the location of a collocated cup anemometer at 103 m height on the NOAH meteorological mast, using an accumulation time of 1000 ms. The scan configuration for this phase is schematically depicted in Figure 1b and summarized in Table 1. To ensure consistency with the temporal sampling of the multi-point scanning configuration used in the second phase, the northern beam was resampled to an effective sampling frequency of 1/12 Hz, corresponding to four dual-Doppler points. This established the baseline uncertainty (with cup as the reference) of wind speed and turbulence intensity derived from the multi-point dual-Doppler reconstruction under conditions of negligible horizontal separation (collocated) between the range gates.

Phase 2 of the experiment was designed to investigate the influence of horizontal separation between the two range gates used for the dual-Doppler reconstruction. During this phase, AUDRA and SL_S operated in continuous staring mode at 1 Hz, while SL_N performed a four-position stop-and-stare azimuth scan. One azimuth position intersected the southern staring beam, providing an internal collocated reference point, while the remaining three azimuth positions introduced increasing horizontal separations, without vertical separation, between the gates used for reconstruction. The effective sampling frequency of the multi-point configuration corresponded to a revisit time of 12 s for SL_N. The azimuth angles were selected to yield horizontal separation distances of approximately 500, 1000, and 1500 m relative to the intersection point, while the elevation angles were chosen to ensure no vertical separation to the intersection point (at 80 m height), also maintaining its longitude. This experimental design enabled a controlled assessment of whether increasing spatial separation introduces additional uncertainty beyond the baseline level identified in Phase 1. Further details on the scan configurations are provided in Table 1 and Figure 1c.

Table 1. Details of the scanning lidars' scan configurations. The studied range gates for phase 2 are marked in Fig. 1c.

	SL_S	**AUDRA**	**SL_N**	
Phase	1 & 2	1 & 2	1	2
Start date	2025-05-04	2025-05-02	2025-05-09	2025-07-04
End date	2025-08-21	2025-08-21	2025-07-03	2025-08-19
Scan mode	Fixed	Fixed	Fixed	Stop and stare
Elevation (°)	0.96	0.74	0.74	[0.75, 0.70, 0.65, 0.60]
Azimuth (°)	69.3	129.10	129.09	[129.09, 133.16, 136.71, 139.80]
Acc. Time (ms)	1000	1000	1000	1000
Probe length (m)	100	100	100	100
Studied range gate (m)	5342 (phase 1), 4042 (phase 2)	6808	6807	[5107, 5457, 5857, 6257]
Hor. separation to the studied range gate of SL_S (m)	-	Collocated	Collocated	[1495.88, 978.01, 479.57, Collocated]
Revisit time (s)	1	1	1	12
Final # of 10-min reconstructed samples	-	2182 *(phase 1)*	2999	[4723, 4552, 4385, 4129]

https://doi.org/10.5194/wes-2026-99
Preprint. Discussion started: 15 July 2026

2.2 Dual-Doppler Reconstruction

To reconstruct the wind statistics from the line of sight measurements, we follow this procedure: First, the high frequency raw LOS data from each lidar go through a quality filter, which is described in Section 2.2.1. Then, the reconstruction described in section 2.2.2 is applied to the desired range gates if the two LOS velocities are within 1 second intervals to ensure synchronization. The 10-min mean wind speed and TI are considered valid if the recovery rate, defined as the ratio between the number of available samples and the maximum possible number of samples within the averaging period, reaches at least 65%. This corresponds to a minimum of 390 samples for 1 Hz data and 32 samples for 1/12 Hz data for the calculation of first- and second-order statistics. A sensitivity study was performed to evaluate the impact of recovery-rate and CNR filtering on the reconstructed wind statistics. Both criteria were effective in removing low-quality measurements. The recovery-rate threshold was therefore set to 65% based on the resulting reconstruction performance, while the selected CNR thresholds are described in the following section.

2.2.1 LOS processing

To reconstruct wind parameters, the two LOS signals must be filtered to ensure adequate signal quality. Formal standards for scanning lidars are still under development (cf. IEC 61400-50-5). Carrier-to-noise ratio (CNR) thresholds in the range of approximately –24 dB to –30 dB have commonly been adopted in the literature as a lower cutoff for data acceptance. Floors et al. (2016) accepted measurements with CNR > –26.5 dB using long-range WindScanner systems. Using the same type of scanning lidars, Peña and Mann (2019) compared turbulence reconstructed values against sonic anemometer data by accepting LOS data with CNR values between –25 dB and –5 dB, and additionally de-spiking the LOS time series prior to reconstruction. All 10-min values with a recovery rate of less than 83% were rejected. More advanced, dynamic filtering approaches were proposed by Beck and Kühn (2017) and applied to data collected by a pair of WindCube Scan 200S systems at ranges of 1.6 km and 1.5 km during a near-shore offshore campaign in Japan (Shimada et al., 2022, 2025). In Shimada et al. (2025), an additional recovery-rate filter of 10% was also applied. However, the dynamic filtering methodology is developed based on mean wind speed in Beck and Kühn (2017) and is one of the best performing approaches among the studied filters, but this method did not perform well in terms of standard deviation of wind speed, which is where the focus of this study lies. In our analysis, both the CNR threshold and recovery-rate filtering are found to be effective in removing low-quality data. After applying the manufacturer-provided STATUS flag, we adopt a more general approach by using a relatively permissive lower CNR threshold of -29 dB and a higher threshold of -7 dB.

Following the signal-based quality filtering, the data are resampled to ensure consistent sampling rates between the two phases. Specifically, the 1 Hz dataset from Phase 1 is resampled to 1/12 Hz on a regular 12 s temporal grid. The line-of-sight measurements from SL_N are then selected within a ± 0.5 s window around each 12 s timestamp. A rolling 3σ filter is subsequently applied to remove outliers. A recovery-rate criterion of 65% is used to determine which 10-min statistics are accepted after reconstruction. This corresponds to a minimum number of samples depending on the sampling frequency, i.e., at least 390 samples for a 1 Hz dataset and 32 samples for a 1/12 Hz dataset.

https://doi.org/10.5194/wes-2026-99
Preprint. Discussion started: 15 July 2026

Open Access WIND ENERGY SCIENCE DISCUSSIONS

2.2.2 Collocated reconstruction

The projection of a three-dimensional wind vector onto the LOS direction is given by:

$$v_r = usin(\theta)cos(\phi) + vcos(\theta)cos(\phi) + wsin(\phi), \tag{1}$$

where v_r is the line of sight velocity, θ is the scan azimuth starting from the north in a clockwise direction, ϕ is the scan elevation, and u, v and w are the zonal, meridional and vertical velocity in a fixed reference coordinate system, respectively.

Assuming $wsin(\phi)$ is negligible, we reconstruct the wind components using the two filtered LOS measurements as follows:

$$\mathbf{v} = \mathbf{M}^{-1}\mathbf{v_r}, \tag{2}$$

where

$$\mathbf{v_r} = \begin{bmatrix} v_{r_1} \\ v_{r_2} \end{bmatrix}, \quad \mathbf{v} = \begin{bmatrix} u \\ v \end{bmatrix}, \quad \mathbf{M} = \begin{bmatrix} \sin(\theta_1)\cos(\phi_1) & \cos(\theta_1)\cos(\phi_1) \\ \sin(\theta_2)\cos(\phi_2) & \cos(\theta_2)\cos(\phi_2) \end{bmatrix}.$$

We calculate the horizontal mean wind speed ($\overline{U}$) and TI for a 10-min period, as commonly used in wind resource assessment applications. The horizontal wind speed (U) and TI are defined as:

$$U = \sqrt{u^2 + v^2}, \quad TI = \frac{\sigma(U)}{\overline{U}} \tag{3}$$

We also calculate the representative TI from the reconstructed and cup TI for each wind speed bin i. Representative TI is the 90th percentile, calculated commonly using the mean and standard deviation of TI for the bin i, assuming a Gaussian distribution (IEC 61400-1, 2019; St. Pé et al., 2021):

$$TI_{rep,i} = TI_{mean,i} + 1.28 \times TI_{std,i} \tag{4}$$

2.2.3 Non-collocated reconstruction

The non-collocated reconstruction uses two gates that are not collocated in space (but in time) for the reconstruction, as its name suggests. The reconstruction itself follows the standard approach described in section 2.2.2.

Three non-collocated pairs are studied in detail to quantify the impact of separation on the uncertainty, listed in Table 1 and marked in Figure 1c. The only difference between the reconstruction of these three pairs and a collocated pair is the horizontal separation between the range gates. The time synchronization is also the same, as the southern beam operates in stare mode and has a maximum tolerance of 1 s with the associated non-collocated LOS.

To further study the spatial variations beyond DD1-3, we use the following algorithm to identify the two non-collocated range gates for reconstruction: For each range gate of the southern lidar, we search for the closest northern gate in the vertical

https://doi.org/10.5194/wes-2026-99
Preprint. Discussion started: 15 July 2026

direction, with a maximum allowed vertical separation of 0.5 m, which is justified based on the pointing accuracy. If the horizontal distance between these two gates is below 1 km, we reconstruct the wind components and visualize them at the position of the northern beam (see Fig. B2 (a-c) as an example). As the two north-most turbines are in the line of sight direction of all three lidars, we only apply the reconstruction at the west side of longitude = -1.419 to avoid the turbine effect on the reconstructions.

2.2.4 Second-Order Statistics

The covariance of the reconstructed wind vector given by equation 2 follows:

$$\mathbf{\Sigma_v} = \mathbf{M}^{-1}\mathbf{\Sigma_{v_r}}(\mathbf{M}^{-1})^T, \tag{5}$$

where the covariance matrix of the line-of-sight velocities is defined as

$$\mathbf{\Sigma_{v_r}} = \begin{bmatrix} \sigma^2(v_{r_1}) & \sigma(v_{r_1}, v_{r_2}) \\ \sigma(v_{r_1}, v_{r_2}) & \sigma^2(v_{r_2}) \end{bmatrix}. \tag{6}$$

The variances and covariance are computed from time series as

$$\sigma^2(v_{r,i}) = \left\langle (v_{r_i} - \langle v_{r_i}\rangle)^2 \right\rangle, \tag{7}$$

$$\sigma(v_{r_1}, v_{r_2}) = \langle (v_{r_1} - \langle v_{r_1}\rangle)(v_{r_2} - \langle v_{r_2}\rangle)\rangle, \tag{8}$$

where $\langle\cdot\rangle$ denotes temporal averaging. The inverse of $\mathbf{M}$ is given by

$$\mathbf{M}^{-1} = \frac{1}{\cos(\phi_1)\cos(\phi_2)\sin(\theta_1 - \theta_2)} \begin{bmatrix} \cos(\theta_2)\cos(\phi_2) & -\cos(\theta_1)\cos(\phi_1) \\ -\sin(\theta_2)\cos(\phi_2) & \sin(\theta_1)\cos(\phi_1) \end{bmatrix}. \tag{9}$$

Defining

$$D = \cos(\phi_1)\cos(\phi_2)\sin(\theta_1 - \theta_2),$$

the variances and covariance of the reconstructed wind components are

https://doi.org/10.5194/wes-2026-99
Preprint. Discussion started: 15 July 2026

$$\sigma^2(u) = \frac{1}{D^2}\Big[\cos^2\theta_2\cos^2\phi_2\,\sigma^2(v_{\mathrm{r}_1}) + \cos^2\theta_1\cos^2\phi_1\,\sigma^2(v_{\mathrm{r}_2}) \\ - 2\cos\theta_1\cos\theta_2\cos\phi_1\cos\phi_2\,\sigma(v_{\mathrm{r}_1},v_{\mathrm{r}_2})\Big], \tag{10}$$

$$\sigma^2(v) = \frac{1}{D^2}\Big[\sin^2\theta_2\cos^2\phi_2\,\sigma^2(v_{\mathrm{r}_1}) + \sin^2\theta_1\cos^2\phi_1\,\sigma^2(v_{\mathrm{r}_2}) \\ - 2\sin\theta_1\sin\theta_2\cos\phi_1\cos\phi_2\,\sigma(v_{\mathrm{r}_1},v_{\mathrm{r}_2})\Big], \tag{11}$$

$$\sigma(u,v) = \frac{1}{D^2}\Big[-\sin\theta_2\cos\theta_2\cos^2\phi_2\,\sigma^2(v_{\mathrm{r}_1}) - \sin\theta_1\cos\theta_1\cos^2\phi_1\,\sigma^2(v_{\mathrm{r}_2}) \\ + (\sin\theta_2\cos\theta_1 + \sin\theta_1\cos\theta_2)\cos\phi_1\cos\phi_2\,\sigma(v_{\mathrm{r}_1},v_{\mathrm{r}_2})\Big]. \tag{12}$$

Using the identity

$$\sin\theta_2\cos\theta_1 + \sin\theta_1\cos\theta_2 = \sin(\theta_1+\theta_2),$$

the covariance simplifies to

$$\sigma(u,v) = \frac{1}{D^2}\Big[-\sin\theta_2\cos\theta_2\cos^2\phi_2\,\sigma^2(v_{\mathrm{r}_1}) - \sin\theta_1\cos\theta_1\cos^2\phi_1\,\sigma^2(v_{\mathrm{r}_2}) + \sin(\theta_1+\theta_2)\cos\phi_1\cos\phi_2\,\sigma(v_{\mathrm{r}_1},v_{\mathrm{r}_2})\Big]. \tag{13}$$

To obtain a clearer view of how azimuthal geometry and LOS second-order statistics contribute to the reconstructed wind moments, we assume small elevation angles and approximate $\cos\phi_i \approx 1$. This yields a simplified form:

$$D \approx \sin(\theta_1-\theta_2), \tag{14}$$

and the components of the covariance matrix become:

$$\sigma^2(u) = \frac{1}{\sin^2(\theta_1-\theta_2)}\Big[\cos^2\theta_2\,\sigma^2(v_{\mathrm{r}_1}) + \cos^2\theta_1\,\sigma^2(v_{\mathrm{r}_2}) - 2\cos\theta_1\cos\theta_2\,\sigma(v_{\mathrm{r}_1},v_{\mathrm{r}_2})\Big], \tag{15}$$

$$\sigma^2(v) = \frac{1}{\sin^2(\theta_1-\theta_2)}\Big[\sin^2\theta_2\,\sigma^2(v_{\mathrm{r}_1}) + \sin^2\theta_1\,\sigma^2(v_{\mathrm{r}_2}) - 2\sin\theta_1\sin\theta_2\,\sigma(v_{\mathrm{r}_1},v_{\mathrm{r}_2})\Big], \tag{16}$$

$$\sigma(u,v) = \frac{1}{\sin^2(\theta_1-\theta_2)}\Big[-\sin\theta_2\cos\theta_2\,\sigma^2(v_{\mathrm{r}_1}) - \sin\theta_1\cos\theta_1\,\sigma^2(v_{\mathrm{r}_2}) + \sin(\theta_1+\theta_2)\,\sigma(v_{\mathrm{r}_1},v_{\mathrm{r}_2})\Big]. \tag{17}$$

Note that these second-order statistics can directly be calculated from the highly resolved reconstructed u and v. The derived formulation of the second-order statistics based on the scan configuration and LOS statistics assist in interpreting the results of

https://doi.org/10.5194/wes-2026-99
Preprint. Discussion started: 15 July 2026

non-collocated reconstruction. All three second-order turbulence quantities, i.e. σ_u^2, σ_v^2, and σ_{uv}, contribute to the variance of the horizontal wind speed and therefore propagate directly into the TI. This highlights that uncertainties in TI reconstruction are not only controlled by the variance magnitude itself, but also by the covariance structure between the reconstructed wind components. A similar dependency of TI reconstruction on the covariance structure and turbulence anisotropy has recently been discussed in Archer (2025).

$$\sigma_U^2 = \left(\frac{\partial U}{\partial u}\right)^2 \sigma_u^2 + \left(\frac{\partial U}{\partial v}\right)^2 \sigma_v^2 + 2\left(\frac{\partial U}{\partial u}\frac{\partial U}{\partial v}\right)\sigma_{uv} \tag{18}$$

Since

$$U = \sqrt{u^2+v^2},$$

the partial derivatives are

$$\frac{\partial U}{\partial u} = \frac{u}{\sqrt{u^2+v^2}}, \qquad \frac{\partial U}{\partial v} = \frac{v}{\sqrt{u^2+v^2}}.$$

Substituting into the propagation equation yields

$$\sigma_U^2 = \frac{u^2}{u^2+v^2}\sigma_u^2 + \frac{v^2}{u^2+v^2}\sigma_v^2 + \frac{2uv}{u^2+v^2}\sigma_{uv}. \tag{19}$$

The weighting of the individual terms depends on the mean wind direction through the relative magnitudes of u and v. Consequently, the sensitivity of TI to reconstruction errors in σ_u^2, σ_v^2, and σ_{uv} varies with flow direction and atmospheric conditions.

2.3 Atmospheric stability

We use the Bulk Richardson Number (Ri_b) to inform about the atmospheric stability conditions during the campaign, defined as (Stull, 1988):

$$Ri_b = \frac{g\Delta\theta_v\Delta z}{\theta_v U_z^2}. \tag{20}$$

In this study, we examine the dependence of the reconstructions on bulk Richardson number values, rather than classifying stability conditions based on fixed thresholds. We calculate the Ri_b between sea level and 35 m above mean sea level using data from the wave buoy and the NOAH met mast.

https://doi.org/10.5194/wes-2026-99
Preprint. Discussion started: 15 July 2026

2.4 Atmospheric conditions

The atmospheric conditions during both Phase 1 and Phase 2 are summarized in Fig. 2 using concurrent measurements from the wave buoy and the NOAH met mast. Northerly inflow directions (Sector A) are predominantly associated with unstable to near-neutral stratification and comparatively low TI levels. These conditions correspond to offshore flow with long marine fetch and limited upstream flow obstruction, resulting in relatively homogeneous atmospheric conditions.

Two pronounced TI peaks are observed in Sector B, which can likely be attributed to the influence of the two neighboring wind turbines located upstream of the measurement site for these inflow directions. In contrast, winds advected from the coastline (primarily Sector D) exhibit elevated TI levels and are predominantly associated with stable stratification. These conditions are consistent with increased flow heterogeneity induced by coastal roughness transitions and developing internal boundary-layer effects.

The wind rose in Fig. 2(c) further indicates two dominant inflow regimes during the campaign: northerly winds, which occurred primarily during Phase 1, and westerly to southwesterly winds, which dominated during Phase 2. Both regimes exhibit comparable wind-speed distributions, while the highest wind-speed occurrences are associated with a storm event named Floris, which impacted the site on 4 August 2025.

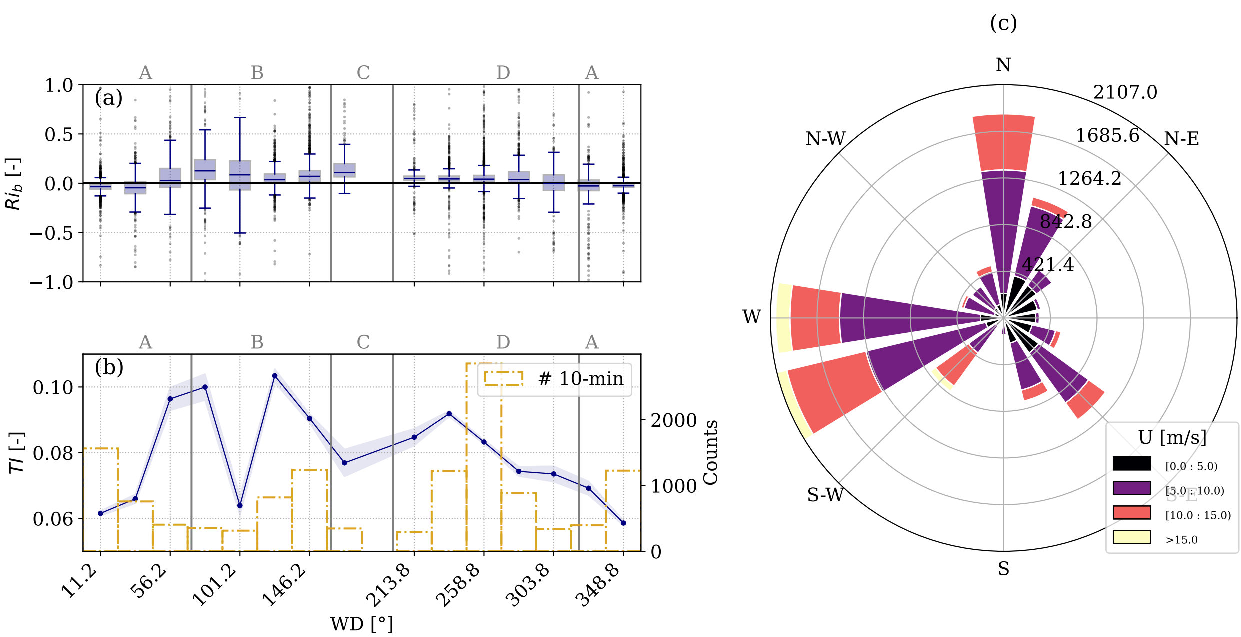

Figure 2. The atmospheric conditions between 2025-05-02 and 2025-08-21 at the NOAH met mast. Panel (a) and (b) show the Ri_b and TI derived from the cup at 103 m for different wind directions, respectively. The wind direction is provided by the wind vane at 101 m and the shaded area marks the standard error for each direction bin. Sections A-D are later used in the discussion and also shown in Figure 1. Panel (c) shows the wind rose for the same period.

https://doi.org/10.5194/wes-2026-99
Preprint. Discussion started: 15 July 2026

2.5 LES case study

2.5.1 Case study description

To gain further insight into the turbulence structure of the site and to evaluate the proposed non-collocated reconstruction strategy, a large-eddy simulation (LES) was performed for two specific days of the campaign. This LES is also used to assess whether non-collocated beam configurations can reproduce the spatial variability of wind speed and turbulence intensity represented in the LES fields.

The case study was selected based on the following criteria: good lidar data availability; a good match between observations and the mesoscale forcing model; a high level of turbulence; and a relatively constant wind direction that would allow the study domain to be free from the influence of wind turbine wakes (i.e. avoiding winds from the east and south-east). Based on these criteria, it was decided to conduct the LES for the two days between 5 and 6th of August 2025. On these days, the wind steadily blows from the west with a speed of 8 to 16 m.s^{-1} at 80 m a.s.l. off the coast of Blyth (Fig. B1). These two days are clear summer days with strong diurnal surface warming, which leads to an unstable and turbulent atmospheric boundary layer (ABL) over land but stable conditions over the sea during the day. The Bulk Richardson Number close to the NOAH met mast is found between -0.05 and 0.1. The turbulence at approximately 5 km off the coast of Blyth is therefore partly due to the advection of turbulence generated over land. During the night, the ABL becomes stable and turbulence levels decrease. These periods are not included in the following analysis due to the model's insufficient turbulence resolution capabilities, in such stable contexts as explained below.

2.5.2 LES model and setup

The LES is performed with the Meso-NH v5.7.2 coupled surface–atmosphere model (Lac et al., 2018). Meso-NH is a non-hydrostatic, limited-area model designed to be used at both the mesoscale and the LES scale. To model real weather situations at the LES scale using Meso-NH, a dynamical downscaling approach is employed, beginning at the mesoscale. This is achieved using a grid-nesting approach with three domains. Figure 3 shows the different domains used and the topography of the region. The largest domain covers northern England and part of the western North Sea. It has a horizontal resolution of 1 km. The second domain has a horizontal resolution of 200 m. The third and final domain has a horizontal resolution of 40 m, enabling it to explicitly resolve the largest eddies of turbulence and be categorised as LES. The simulations use a stretched vertical resolution with 90 levels, with the finest resolution near the ground. The configuration in question features 60 levels below 2000 m, with its lowest level at 2 m, making it specifically adapted to the study of the ABL.

https://doi.org/10.5194/wes-2026-99
Preprint. Discussion started: 15 July 2026

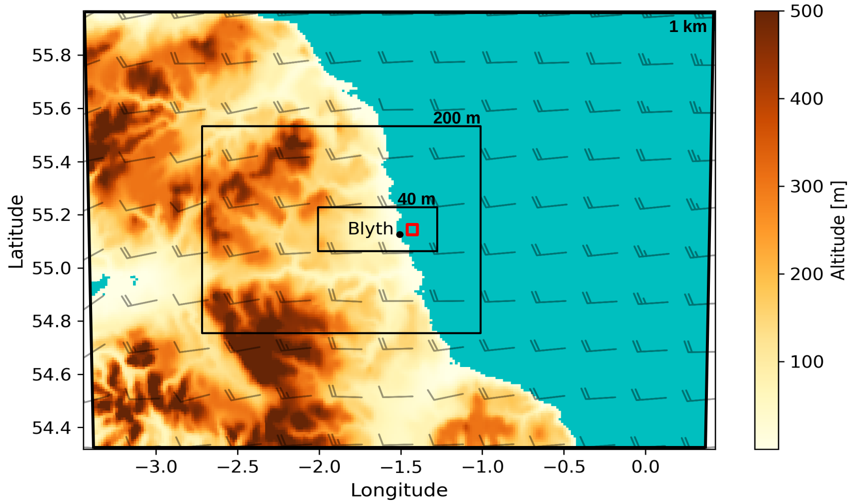

Figure 3. Nested domains used for dynamical downscaling in Meso-NH. Each domain's resolution is given in its lower-right corner. The red subdomain is used for high-frequency outputs and corresponds to Figure 4. The barbs represent the mean horizontal wind at 80 m a.s.l. during the case study.

The dynamic core employs a grid-point Eulerian approach, utilizing a fourth-order centered advection scheme for wind variables. This setup offers a high effective model resolution, roughly equivalent to five times the horizontal grid resolution (Ricard et al., 2013), i.e. approximately 200 m. Consequently, turbulent structures smaller than 200 m are likely to be under-resolved. These smaller structures must therefore be represented at the subgrid scale with the appropriate parameterization. This subgrid turbulence is parameterized using the scheme of Cuxart et al. (2000) combined with the mixing length of Honnert et al. (2021). The surface model incorporated into Meso-NH v5.7.2 is SURFEX v8.1 (Masson et al., 2013). In the present study the sea surface is modelled using simple parameterizations. The sea-surface temperature is prescribed and taken from the European Center for Medium-range Weather Forecast (ECMWF) analysis. The roughness length is calculated with the Charnock formula (Charnock, 1955), and the surface heat fluxes are calculated using COARE3 parameterization (Fairall et al., 2003; Brossier et al., 2009).

The Meso-NH mesoscale simulation is first initialized with the ECMWF analyses, and is then forced along its lateral boundaries by these analyses. Each nested domain is then forced to its boundaries by the larger domain, up to the LES. The LES runs with a time step of 1 s. It is configured to yield mean turbulent statistics every half an hour over the full LES domain and the 3D wind components every three seconds over the subdomain of interest for this study. This subdomain of interest is shown in Figure 4. This allows the application of the proposed dual-Doppler lidar reconstruction strategy to be investigated for a greater number of points in space.

https://doi.org/10.5194/wes-2026-99
Preprint. Discussion started: 15 July 2026

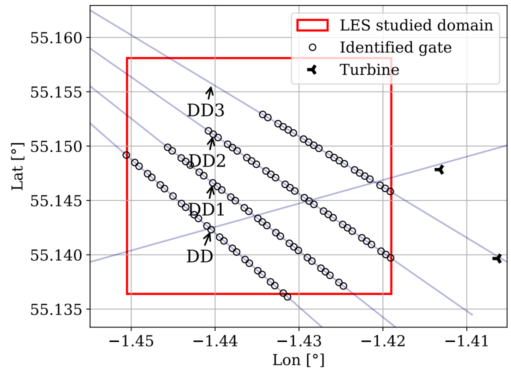

Figure 4. The sub-domain of interest in this study. The coordinates of the domain are: lon = [-1.4505, -1.4190], lat = [55.1364, 55.1581] at height 80 m a.s.l. The markers show the lidar range gates found using the non-collocated reconstruction algorithm.

2.5.3 LES validation

Special attention is given to ensuring the turbulence is generated properly in the LES data used in this study. This type of LES is constrained by the flow modeled in larger simulation domains, so it cannot use periodic conditions to facilitate turbulence generation. In this context, the resolved turbulence progressively develops in the western part of the LES domains and, on average, reaches equilibrium by the middle of the domain. A common norm for judging LES quality is to consider that 80% of the turbulence must be explicitly resolved by the simulation (Ahmadi-Baloutaki and Aliabadi, 2021). If this threshold is not met by the middle of the domain (i.e. 4 km upwind of the coast), the corresponding LES time periods are excluded from the analysis. This filter retains only the times between 07:00 and 12:00 UTC on 5 August and between 07:00 and 19:00 UTC on 6 August.

The resulting 10-minute time series are shown in Fig. B1. To further assess the representativeness of the LES flow, the Power Spectral Density (PSD) of the horizontal wind speed is analyzed. As illustrated in Fig. 5, the LES spectra are in good agreement with the collocated lidar-based reconstruction, demonstrating a consistent representation of turbulent scales. In particular, both datasets capture the inertial subrange with comparable spectral characteristics. This agreement indicates that the LES fields provide a physically consistent reference for spatial extrapolation.

https://doi.org/10.5194/wes-2026-99
Preprint. Discussion started: 15 July 2026

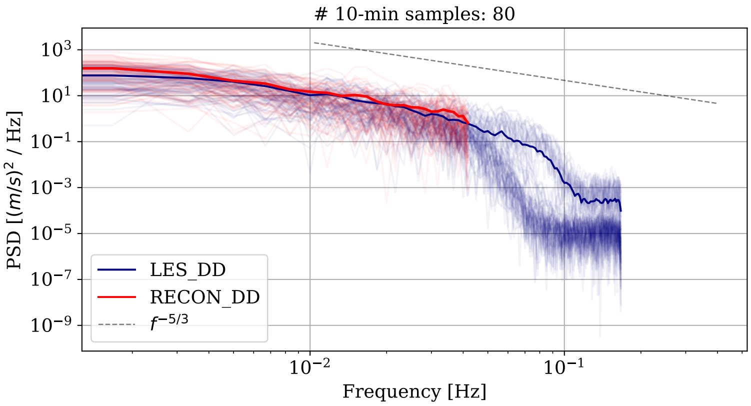

Figure 5. PSD comparison of 80 concurrent 10-min samples from LES and SL_N-SL_S reconstruction at DD. Each 10-min PSD is implemented using welch method with detrended signal and a window size of 10-min.

2.6 Objectives and validation concepts

To address the three research questions, we define three validation exercises, summarized in Table 2.

First, we determine the measurement capability of collocated DSL reconstruction by comparing two reconstructed datasets (using three scanning lidars) against cup anemometer measurements. This provides a baseline estimate of the collocated DSL measurement uncertainty.

Secondly, we compare the collocated (DD point in Figure 1c) with the non-collocated (DD1-3 in Figure 1c) reconstructions and quantify the resulting deviation. Given the scan configuration, the deviation arises solely from the horizontal separation between the range gates. In the absence of an in-situ reference for this phase, we rely on the collocated DSL uncertainty results from Phase 1 to determine the separation distance at which the (collocated) measurement uncertainty is reached. Deviations exceeding this level are then interpreted as potential signatures of spatial variability.

Finally, we apply the non-collocated reconstruction beyond the identified separation limit to investigate whether the resulting spatial variations can be attributed to physically meaningful flow structures, using LES data as a reference for comparison.

https://doi.org/10.5194/wes-2026-99
Preprint. Discussion started: 15 July 2026

Table 2. Validation/verification exercises and objectives

Phase	Objective	Reference dataset	Test dataset	Reconstructions
1	Baseline uncertainty of multi-point collocated DSL reconstruction	Cup anemometer	Collocated reconstruction in the vicinity of the cup anemometer (resampled to 1/12 Hz)	AUDRA-SL_S , SL_N-SL_S
2	Impact of separation distance on uncertainty	Collocated reconstruction at DD	Non-collocated reconstruction at DD1–DD3	SL_N-SL_S
2	Spatial variability of wind speed and TI	LES in the measurement domain (feasibility analysis)	Non-collocated reconstruction over the measurement domain	SL_N-SL_S

In the absence of IEC standards specifically addressing scanning lidar, and inspired by St. Pé et al. (2021) and Kelberlau et al. (2023), whose suggested acceptance thresholds are partially adopted in industrial applications for TI performance, we use the Mean Bias Error (MBE) and Root Mean Squared Error (RMSE) to quantify the uncertainty of the reconstructed values.

In the following, the formulas for MBE and RMSE are shown for TI for bin i; the same definitions are applied to wind speed and representative TI. The choice of reference dataset (denoted as *ref*) is detailed in Table 2.

An acceptance threshold of 0.01 for TI MBE is used for reference, following the recommendation of Kelberlau et al. (2023).

$$\mathrm{TI}_{\mathrm{RMSE},i} = \sqrt{\frac{1}{N_i}\sum_{n=1}^{N_i}(\mathrm{TI}_{\mathrm{recon},i} - \mathrm{TI}_{\mathrm{ref},i})^2} \tag{21}$$

$$\mathrm{TI}_{\mathrm{MBE},i} = \frac{1}{N_i}\sum_{n=1}^{N_i}(\mathrm{TI}_{\mathrm{recon},i} - \mathrm{TI}_{\mathrm{ref},i}) \tag{22}$$

3 Results

In this section, we begin by quantifying the measurement uncertainty of the traditional collocated DSL reconstruction against a cup anemometer. Subsequently, we present the uncertainty quantification of the non-collocated reconstruction in light of the collocated measurement uncertainty for different separation distances and across different atmospheric conditions. Finally, we present the results on spatial uncertainty for the non-collocated configuration and compare them with the LES fields.

3.1 Collocated DSL

In the first phase of the campaign, the uncertainty of the traditional DSL reconstruction is evaluated using a cup anemometer located in the vicinity of the reconstruction point. Figure 6 shows the performance of two scanning lidar generations relative to

https://doi.org/10.5194/wes-2026-99
Preprint. Discussion started: 15 July 2026

the cup anemometer for each wind speed bin. The SL_N–SL_S reconstruction (both systems v2.1) consistently underestimates both the TI and the representative TI, with a mean bias of -0.01 that remains roughly consistent across all wind speed bins.

In contrast, the AUDRA–SL_S reconstruction (AUDRA v2.0) exhibits a lower mean bias for wind speeds above 5 m/s, but with a stronger dependence on wind speed, indicating higher accuracy on average but reduced consistency across wind speeds (see Figure 6e). Both reconstructions satisfy the TI acceptance threshold of 0.01 for mean bias. However, the SL_N–SL_S reconstruction shows higher precision, with an RMSE below 0.02 as shown in Fig. 6f.

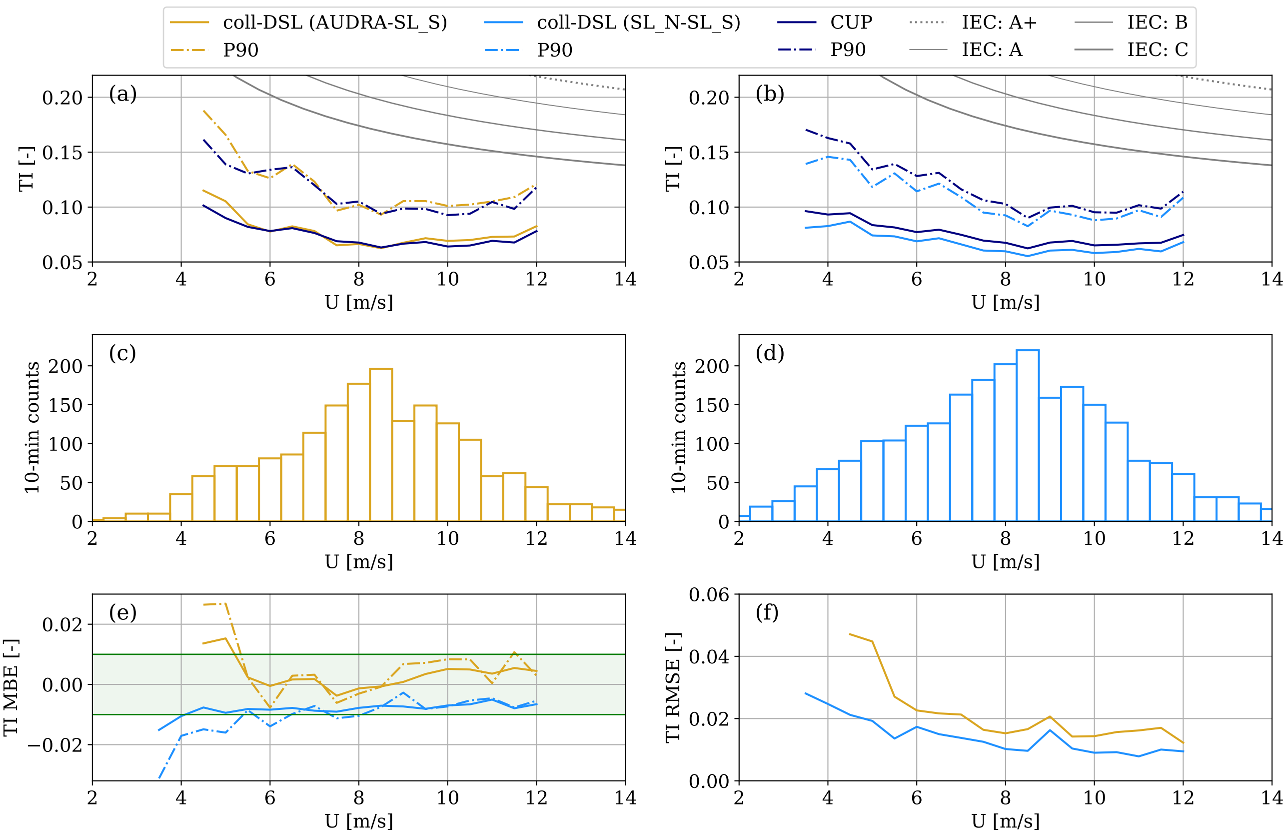

Figure 6. Single point dual-Doppler TI, reconstructed at 1 Hz, for two technology generations compared against the cup. Panel (a) shows the absolute value of TI and the representative TI (P90), reconstructed by AUDRA and SL_S systems for 0.5 m/s wind speed bins. Panel (b) shows the same as panel (a) for SL_N-SL_S reconstruction. Panel (c) and (d) provide the number of samples for each wind speed bin. Panel (e) shows the Mean Bias Error of TI and representative TI for the same bins. Panel (d) depicts the RMSE of TI. Panels a, b, e and f show the parameters and metrics for bins with at least 40 samples.

Due to the higher availability of the SL_N system at higher ranges during Phase 1, this system was a better candidate for performing the non-collocated experiment in Phase 2.

https://doi.org/10.5194/wes-2026-99
Preprint. Discussion started: 15 July 2026

3.1.1 Baseline: Mimicking multi-point Dual-Doppler

As the sampling rate in Phase 2 of the experiment is 12 s for the northern lidar, the same sampling interval is imposed here to determine the baseline uncertainty for Phase 2. After resampling as detailed in section 2.2.1 we observe only a marginal reduction in reconstructed TI and wind speed performance, as indicated in Figure A1 in the Appendix. We use the MBE and RMSE of the resampled dataset as a baseline for Phase 2.

3.2 Non-collocated DSL

We assess the effect of separation distance on TI performance. Figure 7a shows an increase in both TI and representative TI for non-collocated reconstructions compared to the collocated case.

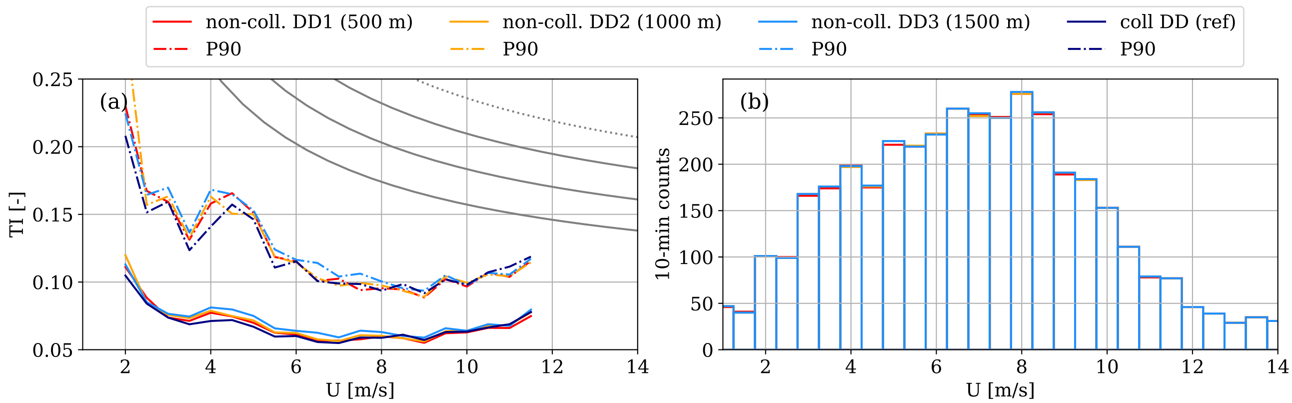

Figure 7. Non-collocated dual-Doppler TI (DD1-3) against collocated dual-Doppler (DD). Panel (a) shows the value of TI and the representative TI (P90) for 0.5 m/s wind speed bins with more than 50 counts and panel (b) shows the number of samples for each bin.

3.2.1 Impact of separation distance

Non-collocated reconstruction leads to systematically elevated TI values, particularly for wind speeds below 8 m/s. The positive bias evident in Figure 8a decreases with increasing wind speed and increases with separation distance across all wind speed bins. The reference TI for the calculation of the error metrics is the collocated TI at DD. The figure also presents the negative bias associated with collocated DSL (from phase 1), with cup as the reference. Precision of non-collocated reconstruction degrades with increasing separation distance, as evidenced by the growing RMSE with distance in Figure 8b.

https://doi.org/10.5194/wes-2026-99
Preprint. Discussion started: 15 July 2026

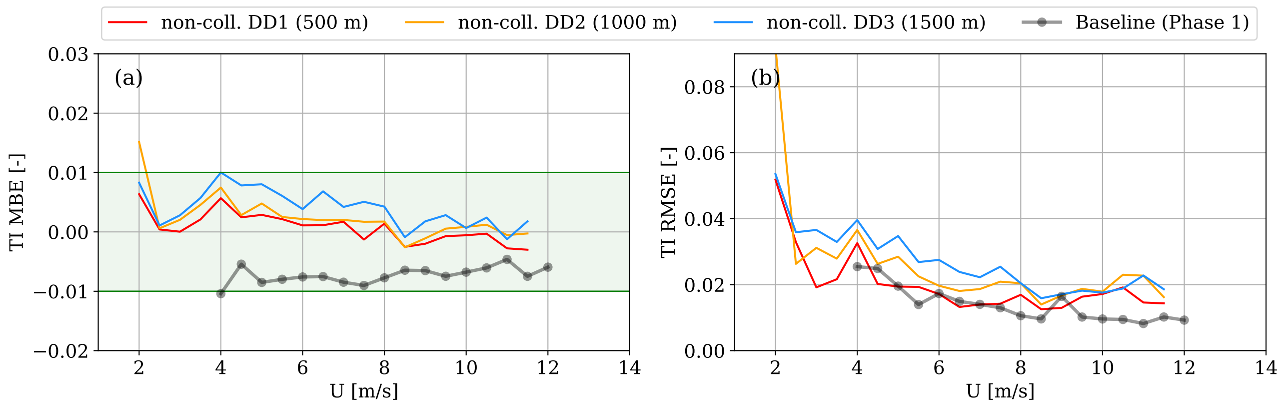

Figure 8. Non-collocated dual-Doppler TI error verified against collocated dual-Doppler (DD). Panels (a) and (b) show the Mean Bias Error and RMSE of TI for 0.5 m/s wind speed bins, respectively. The number of samples for the bins can be found in Fig. 7b.

3.2.2 Impact of atmospheric conditions

The deviations between collocated beams and separated beams as quantified in the last section are sensitive to the atmospheric conditions. In the following we present how the accuracy and uncertainty of mean wind speed as well as turbulence reconstructed by non-collocated beams differs for different wind conditions.

Mean wind speed

The MBE and RMSE between the 10-min wind speed retrieved from the collocated (DD) configuration and the non-collocated configurations (DD1–DD3) are shown in Fig. 9. Panels (a) and (c) present the error metrics for bins containing more than 50 samples, while panels (b) and (d) show the corresponding sample distributions for wind direction and bulk Richardson number, respectively.

Both the bias (MBE) and uncertainty (RMSE) exhibit a clear dependence on wind direction and atmospheric stability. Northerly winds (Sector A) correspond to the most horizontally homogeneous flow conditions, yielding near-zero MBE and low RMSE for all separation distances. Similarly, southerly to west-southwesterly inflow directions remain relatively homogeneous up to approximately 250°, with only minor discrepancies between collocated and non-collocated retrievals. In contrast, two sectors of enhanced sensitivity are identified between approximately 120°–180° and 250°–330°, where both MBE and RMSE increase substantially. The increase in discrepancy with beam separation distance indicates a stronger sensitivity of the reconstructed wind speed to horizontal sampling separation in these sectors.

Regarding atmospheric stability, the second phase of the campaign was dominated by near-neutral and stable conditions, as reflected by the distribution of Ri_b in panel (d). Stable ($Ri_b > 0$) conditions are systematically associated with increased MBE and RMSE. For unstable conditions ($Ri_b < 0$) the errors are similar to the near-neutral conditions ($Ri_b \approx 0$) case when the

https://doi.org/10.5194/wes-2026-99
Preprint. Discussion started: 15 July 2026

non-collocated beams are relatively close (500 and 1000 m apart), but the errors increase when the non-collocated beams are further apart (1500 m).

Among all investigated configurations, the 500 m separation distance (DD1) consistently exhibits the lowest bias and uncertainty, as well as the weakest sensitivity to changing wind conditions. Overall, the results demonstrate that the discrepancy between collocated and non-collocated beam geometries increases with horizontal separation distance.

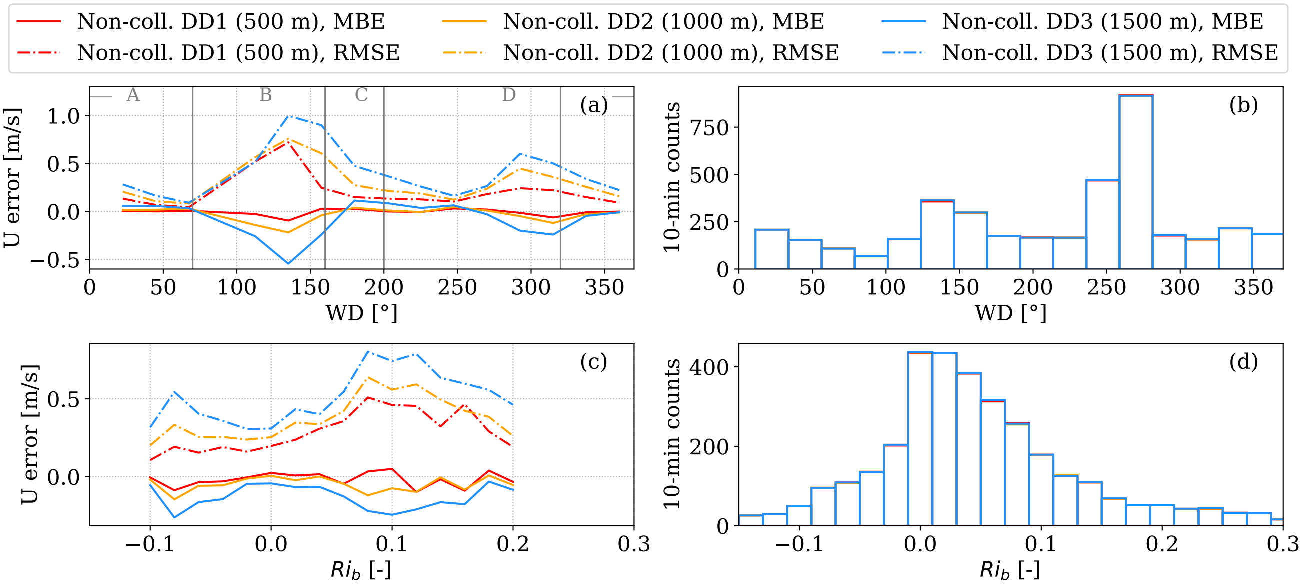

Figure 9. MBE and RMSE between the 10-min mean wind speed retrieved from the collocated dual-Doppler configuration and the non-collocated configurations DD1 (500 m), DD2 (1000 m), and DD3 (1500 m). Panels (a) and (c) show the dependence of the error metrics on wind direction and bulk Richardson number, respectively, considering only bins with more than 50 samples. Panels (b) and (d) present the corresponding sample distributions. The wind direction is measured at DD and grouped into 22.5° degree bins. Vertical gray lines indicate the wind direction sectors discussed in the text.

Turbulence

The horizontal homogeneity of turbulence is assessed by quantifying the error introduced by non-collocated beam configurations for the three horizontal turbulence covariance terms, namely $\sigma^2(u)$, $\sigma^2(v)$, and $\sigma(uv)$. As derived in Eq. 19, all three quantities contribute to the characterization of TI and can therefore propagate into TI uncertainty estimates.

Figure 10 (a–c) presents the errors of the three turbulence terms calculated from the high-resolution reconstructed wind fields, while panels (d–f) show the corresponding reference turbulence quantities obtained from the collocated DD configuration. In general, the results indicate relatively homogeneous turbulence conditions in Sectors A and C, where the errors remain small and only weakly dependent on beam separation distance. In contrast, pronounced inhomogeneities are observed in Sectors B and D for all three turbulence quantities.

https://doi.org/10.5194/wes-2026-99
Preprint. Discussion started: 15 July 2026

eawe european academy of wind energy
Open Access WIND ENERGY SCIENCE DISCUSSIONS

Among the investigated parameters, the error associated with $\sigma^2(v)$ is consistently the largest in magnitude and exhibits the strongest sensitivity to beam separation distance. The most pronounced discrepancies occur for wind directions between approximately $220°$ and $300°$ (Sector D), where the error increases rapidly with separation distance and exceeds $1.5\ \mathrm{m^2\,s^{-2}}$ for the 1500 m configuration. Since this flow sector corresponds to winds advected from the coastal land area, the results suggest that turbulence generated over land remains highly heterogeneous when transported offshore.

The errors in $\sigma^2(u)$ and $\sigma(uv)$ follow similar directional trends but with substantially smaller magnitudes. For $\sigma^2(u)$, the largest discrepancies are again observed in Sector D, coinciding with high values of the reference variance shown in panel (d). In contrast, $\sigma(uv)$ remains comparatively small over all wind directions, in terms of the reference covariance magnitude. However, localized increases are visible in Sectors B and D.

The comparatively low errors observed in Sector A indicate that marine inflow conditions are associated with more horizontally homogeneous turbulence structures. Overall, the results demonstrate that turbulence statistics are substantially more sensitive to beam non-collocation than mean wind speed retrievals, as the non-collocated reconstruction with 500 m separation distance shows more sensitivity of error to wind conditions for turbulence reconstruction than wind speed.

https://doi.org/10.5194/wes-2026-99
Preprint. Discussion started: 15 July 2026

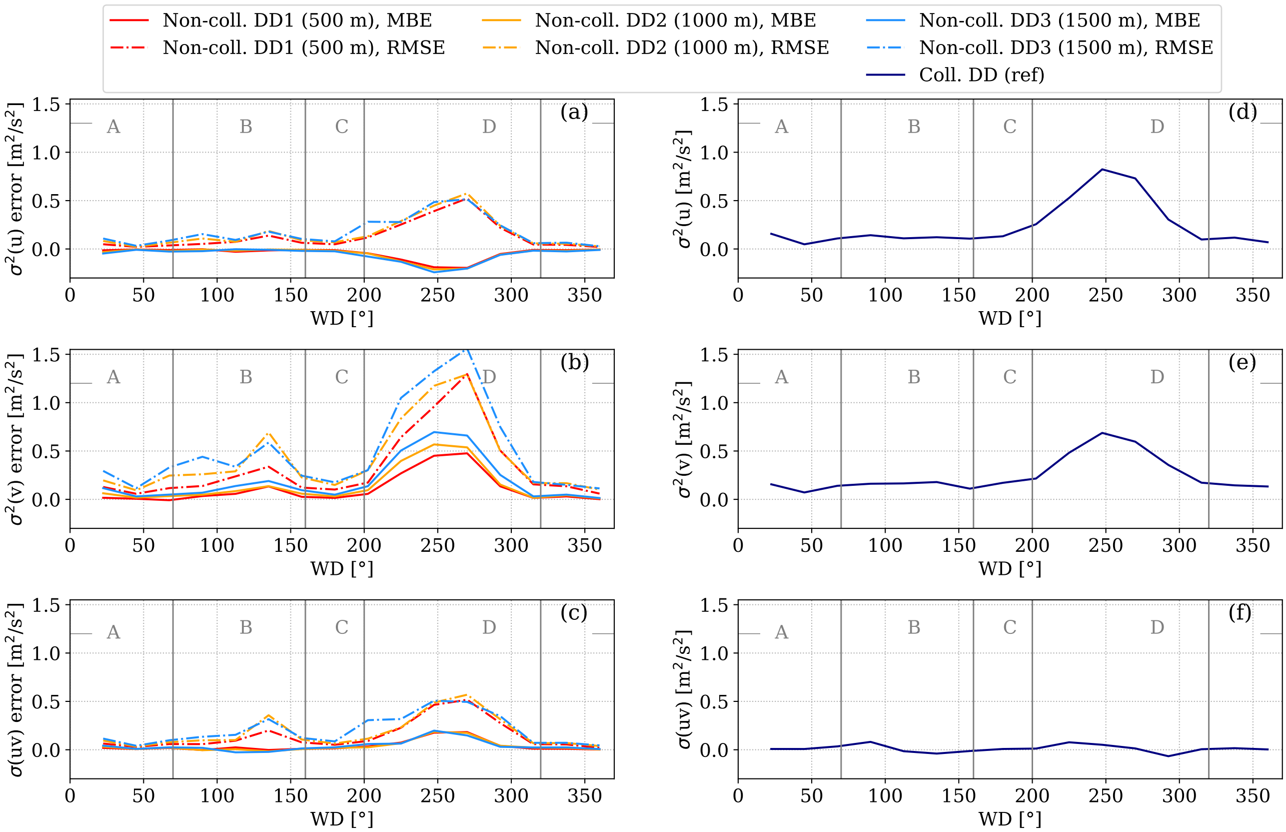

Figure 10. Panels (a–c) show the errors for $\sigma^2(u)$, $\sigma^2(v)$, and $\sigma(uv)$, respectively, for the non-collocated configurations relative to the collocated configuration as a function of wind direction. Panels (d–f) show the corresponding reference turbulence quantities obtained from the collocated DD configuration. The wind direction is measured at DD and grouped into 22.5° bins. The same bins as in Fig. 9 are considered, and only bins with more than 50 samples are included.

To better understand how scan configuration influences the error, we decompose panels (a–c) in Figure 10 into the three contributing terms given in Equations 15–17.

Figure 11 shows the MBE of each term contributing to $\sigma^2(u)$, $\sigma^2(v)$, and $\sigma(u,v)$. The results indicate that, across all three quantities, the third term (associated with the covariance between the two line-of-sight measurements) dominates the overall magnitude of the error. Importantly, this term shows little sensitivity to the separation distance and remains consistently the largest contribution.

In contrast, the first term exhibits a clear dependence on separation distance for both $\sigma^2(u)$ and $\sigma^2(v)$, with consistently higher values observed for $\sigma^2(v)$. The second term also shows a similar pattern, with generally larger contributions in $\sigma^2(v)$ compared to $\sigma^2(u)$, whose overall magnitude remains small across all wind directions.

https://doi.org/10.5194/wes-2026-99
Preprint. Discussion started: 15 July 2026

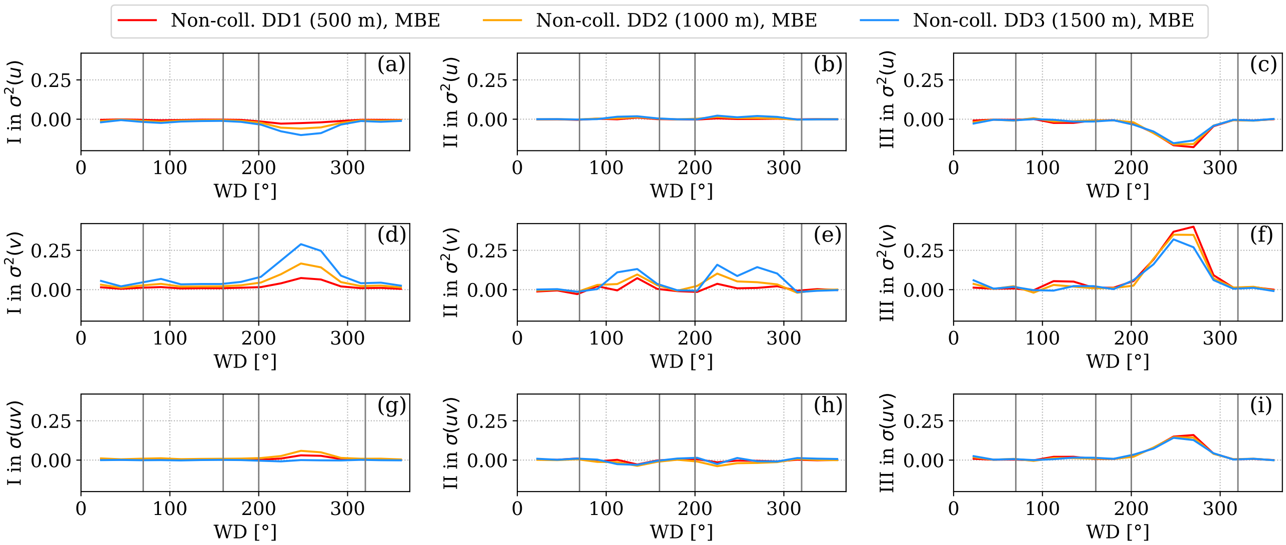

Figure 11. Decomposition of the reconstruction error contributions for the turbulence statistics $\sigma^2(u)$, $\sigma^2(v)$, and $\sigma(uv)$ according to Eq. 15–17, where the data from the southern and northern lidar beams are replaced as v_{r_1} and v_{r_2}, respectively. Rows correspond to the reconstructed turbulence quantities, while columns represent Terms I, II, and III of the decomposition.

3.3 Temporal and spatial variability: LES case study

The results from the DD1–DD3 reconstructions presented in Section 3.2 show that the deviations between collocated and non-collocated reconstructions exceed the measurement uncertainty (derived in Phase 1) for separation distances larger than approximately 500 m. This raises the question of whether these deviations merely represent reconstruction artifacts or whether they are associated with physically meaningful spatial variability of the atmospheric flow. In this section, the apparent spatial variability derived from the non-collocated reconstruction is compared against the intrinsic spatial variability resolved by LES.

The non-collocated reconstruction, applied for a maximum separation distance of 1 km as described in Section 2.2.3, provides spatially distributed flow fields exhibiting finite spatial variability. An example is shown in Fig. B2 for wind speed, wind direction, and TI at a selected time step, together with the corresponding LES fields. Mean and standard deviation values are indicated for comparison. The analysis is restricted to the common spatial domain illustrated in Fig. 4. Overall, the spatial statistics obtained from the non-collocated reconstruction show good agreement with the LES results for the same region. The spatial variability of wind speed is underestimated by the reconstruction, whereas the variability of wind direction is slightly overestimated. In contrast, the spatial variability of TI is reproduced comparatively well.

The average spatial variability across all concurrent time steps is summarized in Table 3 for wind speed and TI. The variability is quantified as the temporal mean of the spatial standard deviation, denoted by $\mu_t(\sigma_s)$, and compared between LES and the non-collocated reconstruction. For wind speed, the reconstructed spatial variability is substantially lower than that resolved

https://doi.org/10.5194/wes-2026-99
Preprint. Discussion started: 15 July 2026

eawe european academy of wind energy
Open Access WIND ENERGY SCIENCE DISCUSSIONS

by LES. In contrast, the spatial variability of TI shows close agreement between the two methods. Despite the differences in variability magnitude, the spatial mean values remain in good agreement overall.

In addition to LES and the non-collocated reconstruction, Table 3 also reports temporal standard deviations, denoted by σ_t, derived from two additional datasets: a conventional collocated AUDRA-SL_S reconstruction based on 1 s sampling near the cup anemometer location, and the cup anemometer measurements themselves. All statistics are computed over a concurrent period shared by the four methods, resulting in 67 10-min samples. For both wind speed and TI, the temporal variability exceeds the corresponding spatial variability by approximately one order of magnitude. Furthermore, the spatially averaged temporal variability derived from the non-collocated reconstruction agrees closely with both the cup measurements and the collocated reconstruction at the met mast.

Table 3. Temporal and spatial variations of wind speed and TI using LES, non-collocated reconstruction, collocated reconstruction and cup anemometer for 67 concurrent 10-min periods between all methods.

		U [m/s]			TI [-]		
Method	Dataset	Spatial var. $\mu_t(\sigma_s(U))$	Temporal var. $\mu_s(\sigma_t(U))$	Mean value $\mu_s(\mu_t(U))$	Spatial var. $\mu_t(\sigma_s(TI))$	Temporal var. $\mu_s(\sigma_t(TI))$	Mean value $\mu_s(\mu_t(TI))$
LES	Spec. domain	0.402	2.649	9.535	0.017	0.022	0.081
Non-coll. Recon.	SL_N-SL_S	0.244	2.575	9.610	0.014	0.029	0.087
Coll. Recon. @ CUP	AUDRA-SL_S	–	2.542	9.520	–	0.029	0.092
In-situ	CUP	–	2.534	9.569	–	0.026	0.092

4 Discussion

To understand the impact of horizontal beam alignment in a dual-Doppler scanning lidar configuration, we adopt a stepwise approach, following Table 2. First, we discuss the measurement uncertainty for the idealized case in which both beams intersect at the measurement point. Then, we evaluate the homogeneity of the flow using the results from separated beams. Finally, the spatial variations are discussed under the most inhomogeneous case and these are compared against LES fields.

4.1 Dual-Doppler performance at extended range

The conventional (collocated) dual-Doppler configuration using WindCube Scan 400S provides accurate and precise 10-min wind speed estimates at distances of 6 – 7 km, using a cup anemometer as reference. The two lidar generations evaluated in this study demonstrate high precision, with RMSE values between 0.166 and 0.249 ms^{-1}, and high accuracy, with linear regression slopes ranging from 0.998 to 1.007 and coefficients of determination (r^2) between 0.990 and 0.996 (results not shown before). Hence the SL_N-SL_S pair passes the acceptance criteria for wind speed required by Carbon Trust (2025). This performance is consistent with the the results shown by Shimada et al. (2022), who evaluated the same technology (type WLS200s) and reported a 0.7% overestimation with an r^2 of 0.996 for 10-min wind speed at ranges of up to 2 km, using a cup anemometer as reference.

Focusing on TI, a different behavior is observed between the two generations. The v2.1 generation (SL_N-SL_S) systematically underestimates both TI and representative TI. In contrast, the v2.0 generation (AUDRA-SL_S) provides a more accurate representation of TI, but with lower precision, exhibiting an RMSE between 0.01 and 0.04, reduced performance compared to an RMSE of 0.01-0.02 for v2.1 generation. For both generations, the TI RMSE decreases with increasing wind speed, which can be attributed to the lower absolute values of TI in this regime.

AUDRA shows reduced data availability compared to SL_N at the met mast range. Examining the CNR as a function of range, the v2.1 systems (SL_N and SL_S) exhibit a slower decay than the v2.0 system on average over Phase 1. This behavior may be partially attributed to differences in hardware such as laser focus settings: in the v2.0 system, these were configured according to the manufacturer's recommended practice, whereas in the newer generation the focus settings are pre-defined and are intentionally non-adjustable by the user.

4.2 Performance of non-collocated dual-Doppler reconstruction

Introducing a horizontal separation between the two dual-Doppler probe volumes degrades the accuracy of the TI reconstruction across all investigated wind-speed bins. However, the magnitude of this degradation must be assessed relative to the baseline measurement uncertainty established for the co-located dual-Doppler configuration in Phase 1.

The TI MBE shown in Fig. 8(a) remains positive across nearly all wind-speed bins, indicating a systematic overestimation of TI by the non-collocated configurations. This trend is consistent with the combined effects of enhanced turbulence variance and the underestimation of mean wind speed at larger beam separation distances, as shown in Section 3.2.2. Despite this tendency, the TI bias remains within the acceptance threshold of ± 0.01 defined by Carbon Trust (2025) for all investigated separation distances. From an application perspective, this positive bias can be regarded as conservative, as it leads to slightly elevated TI estimates and therefore partially offsets the negative TI bias observed for the baseline co-located dual-Doppler measurements relative to the cup anemometer.

The TI RMSE remains comparable to the baseline uncertainty for a beam separation distance of 500 m and wind speeds below 9 ms^{-1}, as shown in Fig. 8(b). Beyond this separation distance, the additional error introduced by the non-collocated reconstruction exceeds the baseline measurement uncertainty across all wind-speed bins. These results suggest that, under the atmospheric conditions encountered during the campaign, a horizontal separation of approximately 500 m can be tolerated without a substantial loss in TI reconstruction performance, whereas larger separations lead to progressively greater deviations from the co-located reference.

4.3 Understanding flow homogeneity for non-collocated DSL

A flow is defined as statistically homogeneous if its statistical properties are invariant under spatial translations (Pope, 2000). This implies that statistical quantities do not depend on absolute position, although instantaneous flow fields may still exhibit

https://doi.org/10.5194/wes-2026-99
Preprint. Discussion started: 15 July 2026

spatial variability. For a fully homogeneous flow, this condition applies to all statistical moments, including the mean velocity field. In contrast, statistically homogeneous turbulence requires only that the statistics of the fluctuating part are spatially invariant (Pope, 2000). In this case, quantities such as the Reynolds stresses do not exhibit spatial gradients, although the mean flow itself may still vary in space.

In this study, we assess flow homogeneity and turbulence homogeneity by examining the spatial dependence of measured statistics, specifically the mean wind and second moments, obtained from reconstructions at different separation distances. If the deviations of the mean are beyond the bounds of measurement uncertainty, the flow homogeneity assumption is considered to be violated. The average reconstructed wind speed is expected to be within the measurement uncertainty for a homogeneous case, and differences beyond the measurement uncertainty can be associated with the flow inhomogeneous or spatial gradients.

For turbulence fields, turbulence homogeneity is required but does not guarantee same statistics for collocated and non-collocated reconstructions. Turbulence de-correlation can also contribute to the deviations. Hence, turbulent homogeneous flows with high correlation distances are favorable conditions for non-collocated reconstruction.

Given the relatively close proximity of the measurement probes to the shore, in order to minimize the influence of large-scale inhomogeneity associated with the coastal transition, the analysis is restricted to a direction parallel to the coastline (here we refer to DD and DD1-3). Please note that no assumption of isotropy – statistical invariance to direction – is imposed in this analysis.

4.3.1 Mean wind homogeneity

Having established an RMSE of approximately $0.17\ \mathrm{m\,s^{-1}}$ for the collocated reconstruction against the cup in Phase 1 (not shown before), Fig. 9 indicates that the mean wind field can be considered horizontally homogeneous in Sector A with good confidence over separation distances of up to 1.5 km. In contrast, the performance of the non-collocated reconstruction degrades in Sector B and partially in Sector D, as reflected by the elevated RMSE values. These sectors are likely influenced by enhanced flow heterogeneity associated with offshore wind turbines and coastal effects, respectively.

The impact of atmospheric stability on the reconstruction error was assessed by comparing the non-collocated dual-Doppler retrievals to the collocated reference in Fig. 9. First, it should be acknowledged that the estimation of the bulk Richardson number (Ri_b) is subject to several limitations. Firstly, the height interval used to determine Ri_b (0–35 m) differs from the reconstruction height (80 m). Secondly, the stability measured at the met mast may not fully represent the boundary-layer conditions of flow advected from the coast, particularly under developing internal boundary-layer conditions. Nevertheless, Ri_b provides a useful first-order metric for assessing the sensitivity of the non-collocated reconstruction to atmospheric stratification.

Near-neutral stratification ($Ri_b \approx 0$ in Fig. 9) provides the most favorable conditions for non-collocated reconstruction. Under neutral conditions, turbulence production is dominated primarily by shear, without strong buoyancy-driven suppression or enhancement. As a result, the flow exhibits relatively large horizontal coherence scales and weak vertical stratification, leading to improved similarity between the spatially separated probe volumes.

https://doi.org/10.5194/wes-2026-99
Preprint. Discussion started: 15 July 2026

For unstable conditions ($Ri_b < 0$), only a limited number of samples are available. Under convective conditions, buoyancy enhances turbulence generation and vertical mixing through energetic three-dimensional eddies. Despite the increased turbulence intensity, the mean wind speed remains comparatively well reproduced, with relatively small systematic bias, as for the neutral cases. The error for a separation distance of 1500 m is larger for unstable conditions than for neutral conditions, while the errors at 500 and 1000 m are of the same order. This suggests that the dominant turbulent structures in unstable conditions do not remain coherent over distances exceeding 1000 m, whereas coherence is maintained over longer distances under neutral conditions.

Moving towards stable conditions ($Ri_b > 0$), the reconstruction uncertainty increases substantially. In stable stratification, buoyancy suppresses vertical motions and limits turbulent mixing, thereby reducing the spatial coherence of the flow. In addition, stable conditions are typically associated with enhanced vertical wind shear. Consequently, even small differences in probe position or effective sampling height between the collocated and non-collocated configurations can produce appreciable deviations in the retrieved wind speed. These effects likely contribute to both the increased bias and RMSE observed under stable conditions. It is notable that the stable conditions are mostly represented by the wind coming from land or passing through the turbines (see Fig. 2(a)).

The performance of the non-collocated configurations degrades progressively with increasing separation distance and consistently exhibits a tendency toward wind-speed underestimation. This behavior may be associated with horizontal gradients in the mean flow along the DD–DD3 transect. Such gradients are plausible because the transect is not perpendicular to the coastline, and DD3 is located closer to the coast than DD due to the curvature of the shoreline. Consequently, the spatially separated beams may sample systematically different flow regimes, violating the homogeneity assumption underlying the dual-Doppler reconstruction. Furthermore, it is expected that the discrepancies between collocated and non-collocated retrievals would decrease for averaging periods longer than 10 min, as temporal averaging would smooth smaller-scale flow variability.

4.3.2 Turbulence homogeneity

We decomposed $\sigma^2(u)$, $\sigma^2(v)$ and $\sigma(uv)$ into the three terms given by Equations 15, 16 and 17. Terms I and II represent the single-beam variance contributions, while Term III represents the cross-beam covariance contribution. This decomposition is motivated by the need to distinguish the effects of scan geometry from those associated with spatial inhomogeneity. Evaluating the turbulence statistics in a fixed Earth-referenced coordinate system also avoids introducing a dependence on the alignment between the beam geometry and the wind direction.

In Terms I and II, the intrinsic LOS variance is weighted by the geometric sensitivity of the dual-Doppler reconstruction. Since the southern lidar samples the same location and retains an unchanged LOS variance ($\sigma^2(v_{r_1})$) across all configurations (collocated and non-collocating), the separation-dependent changes in Term I primarily reflect the changing reconstruction geometry associated with the northern beam angle (θ_2). Increasing the separation distance (moving from DD to DD3) decreases $\cos^2(\theta_2)$ from 0.58 to 0.40 while increasing $\sin^2(\theta_2)$ from 0.42 to 0.60, corresponding to the weighting coefficients of Term I in $\sigma^2(u)$ and $\sigma^2(v)$, respectively. Consequently, the reconstruction exhibits a negative bias contribution in $\sigma^2(u)$ (Fig. 11(a)) and a positive contribution in $\sigma^2(v)$ (Fig. 11(d)).

https://doi.org/10.5194/wes-2026-99
Preprint. Discussion started: 15 July 2026

eawe european academy of wind energy
Open Access WIND ENERGY SCIENCE DISCUSSIONS

This indicates that increasing beam separation in the present configuration progressively rotates the reconstruction sensitivity away from the eastward velocity fluctuations and toward the northward fluctuations in the present scan configurations. The opposite signs observed in the reconstructed $\sigma^2(u)$ and $\sigma^2(v)$ errors therefore originate primarily from the geometric projection of the LOS measurements rather than from a monotonic increase in turbulence inhomogeneity.

The decomposition further demonstrates that the LOS variance itself is not independent of the scan geometry. Since the LOS velocity represents a projection of the horizontal wind vector onto the beam direction, changes in azimuth angle modify not only the geometric weighting coefficients outside the variance terms, but also the turbulence content sampled along each beam. The reconstruction error therefore results from a coupled interaction between atmospheric turbulence statistics and directional projection effects in Term II.

Term II combines the changing projection of the northern lidar with variations in the northern LOS variance ($\sigma^2(v_{\mathrm{r}_2})$) caused by sampling a different spatial location, while keeping the southern beam geometry unchanged (θ_1). Consequently, the observed deviations in Term II cannot be uniquely attributed to spatial inhomogeneity, but instead contain both geometric and physical contributions.

Term III represents the projected LOS covariance contribution and therefore reflects the coherence between the two sampled air volumes. In contrast to Terms I and II, no systematic increase with beam separation distance is observed. This suggests that the dominant separation-dependent deviations in the present experiment are not primarily governed by a monotonic loss of cross-beam covariance. Instead, the wind-direction dependence of Term III appears to be controlled mainly by the angular weighting coefficients together with sector-dependent covariance structures associated with the atmospheric flow.

The largest deviations for all three covariance terms occur in Sector D. This behavior suggests that the atmospheric flow in this sector contains stronger directional variability and anisotropic turbulence structures, which are amplified by the reconstruction geometry. In contrast, the comparatively small deviations observed in Sectors A and C indicate more homogeneous turbulence conditions and a reduced sensitivity of the reconstruction to beam separation distance.

Interestingly, the flow may appear approximately homogeneous with respect to the first-order statistics (mean wind speed), while simultaneously exhibiting significant inhomogeneity in the second-order turbulence statistics. This behavior is evident for wind directions between approximately 200°–250°, where the mean wind speed reconstruction errors remain comparatively small (Fig. 9(a)), whereas the turbulence quantities show substantially enhanced sensitivity to beam separation distance (Fig. 10). This suggests that the large-scale mean flow remains spatially coherent over the investigated separation distances, while the smaller-scale turbulent structures de-correlate more rapidly in space in this sector.

4.4 Spatial uncertainty

We acknowledge the limited sample size of the LES comparison dataset. Nevertheless, the dataset remains highly valuable given the computational expense associated with real-world LES simulations. In particular, the investigated period immediately follows Storm Floris and therefore captures both high wind-speed conditions of up to approximately 15 $\mathrm{m\,s^{-1}}$ as well as more representative operating conditions around 9 $\mathrm{m\,s^{-1}}$.

https://doi.org/10.5194/wes-2026-99
Preprint. Discussion started: 15 July 2026

Table 3 shows that the mean wind speed and TI values agree well across all investigated methods. The LES slightly underestimates the mean TI compared to the measurements, which is expected because the LES-derived TI is based only on the resolved turbulence scales. Approximately 20% of the total turbulence energy is represented by the subgrid-scale model and is therefore not included explicitly in the resolved TI calculation. Including the subgrid contribution would likely further improve the agreement between LES and measurements.

The comparison further demonstrates that the non-collocated reconstruction underestimates the spatial variability of wind speed relative to LES. This indicates that the dual-Doppler reconstruction behaves as a spatial smoothing operator, limiting its ability to fully reproduce the small-scale spatial gradients resolved by LES. Physically, this smoothing behavior arises because the reconstruction combines LOS measurements from spatially separated probe volumes under the assumption of locally homogeneous flow. Consequently, sharp spatial gradients are partially averaged during the reconstruction.

Despite this smoothing effect, the non-collocated reconstruction preserves the mean wind speed remarkably well and reproduces the temporal variability with very good agreement compared to both the collocated reconstruction and the cup anemometer measurements. This is an important result, as it suggests that the additional spatial variability introduced by the non-collocated approach does not simply arise from random reconstruction noise.

In contrast to wind speed, the spatial variability of TI is reproduced comparatively well by the non-collocated reconstruction. Both the mean TI and the spatial TI variability show good agreement with LES while simultaneously retaining realistic temporal variability. This result highlights the potential added value of the non-collocated approach: although the method cannot fully recover the small-scale spatial gradients, it is capable of capturing turbulence heterogeneity over spatial scales comparable with a state-of-the art LES output.

Overall, the results suggest that the deviations introduced by non-collocated reconstruction are not purely reconstruction artifacts, but instead contain information associated with physically meaningful spatial variability of the atmospheric flow. This is particularly relevant for offshore applications, where the assumption of perfectly homogeneous flow is often violated over kilometer-scale distances, even under comparatively ideal marine conditions. The non-collocated approach therefore provides not only a measure of reconstruction uncertainty, but also indirect information about the spatial coherence and heterogeneity of the flow itself.

4.5 Limitations

Several limitations of the present study should be acknowledged. First, the LES comparison is based on a limited number of concurrent samples, reflecting the considerable computational expense associated with real-world LES simulations. In addition, the overall campaign duration was insufficient to comprehensively sample the full range of atmospheric conditions encountered offshore, particularly strongly convective and highly transient boundary-layer regimes.

A further limitation is the absence of an in-situ reference during Phase 2, where the analysis relied on an internal collocated dual-Doppler reference. While this limitation was mitigated through the dedicated Phase 1 validation campaign, an independent reference measurement at the reconstruction range during the non-collocated experiments would further strengthen the

https://doi.org/10.5194/wes-2026-99
Preprint. Discussion started: 15 July 2026

interpretation of the observed deviations. The non-collocated experiment was intentionally conducted at shorter ranges than the Phase 1 in order to maximize data availability, and to minimize the influence of offshore wind turbines on the statistics.

The atmospheric characterization was additionally limited by the available instrumentation. In particular, sonic anemometer measurements would provide a more complete description of the atmospheric boundary layer, including direct measurements of turbulent fluxes and turbulence anisotropy. Such measurements would also enable the application of turbulence spectral tensor models, such as the Mann model, to further investigate the relationship between reconstructed spatial variability and the underlying turbulence structure.

Despite these limitations, the results demonstrate the potential of non-collocated dual-Doppler reconstruction as more than solely a source of reconstruction uncertainty. The observed deviations contain information related to spatial flow variability and turbulence heterogeneity. Future work could therefore exploit non-collocated configurations as a tool for characterizing spatial coherence and atmospheric variability over offshore domains.

5 Conclusions

This study investigated whether strict range-gate intersection is required for dual-Doppler scanning lidar DSL reconstruction of mean wind speed and turbulence intensity under representative offshore conditions. First, the accuracy and uncertainty of the conventional co-located DSL configuration were evaluated against a cup anemometer during an offshore measurement campaign. The results show that the tested v2.1 long-range scanning lidar systems satisfy the Carbon Trust acceptance criteria for mean wind speed and the turbulence intensity criterion for mean bias error of 0.01 at measurement ranges of 6–7 km.

Building on this validation, a non-collocated DSL reconstruction methodology was developed and evaluated, in which synchronized line-of-sight measurements are combined despite horizontal separation between the reconstructed probe volumes. The performance and uncertainty of this approach were assessed using a dedicated measurement phase and a realistic LES case study.

The results demonstrate that a horizontal separation distance of approximately 500 m introduces deviations that remain within the baseline uncertainty of the collocated dual-Doppler reconstruction. Even for larger separation distances up to 1.5 km, the non-collocated configurations remain capable of reproducing representative turbulence intensity values with relatively small systematic bias. This indicates that, under sufficiently homogeneous offshore flow conditions, the assumption of spatially uniform flow remains reasonably valid over substantially separated probe volumes.

The analysis of atmospheric conditions revealed a strong dependence of the reconstruction uncertainty on flow heterogeneity. Two dominant sectors of increased sensitivity were identified: a coastal sector associated with land–sea transition effects and a sector influenced by neighboring offshore wind turbines. In these regions, both wind speed and turbulence errors increased significantly with beam separation distance. In contrast, marine inflow sectors characterized by long offshore fetch and weak turbulence levels exhibited comparatively small deviations between collocated and non-collocated reconstructions.

By decomposing the reconstructed second-order statistics into contributions from the LOS variances and covariance terms, we showed that the covariance term (Term III) dominates the reconstruction error for all three turbulence quantities, namely

https://doi.org/10.5194/wes-2026-99
Preprint. Discussion started: 15 July 2026

$\sigma^2(u)$, $\sigma^2(v)$, and $\sigma(uv)$. The analysis additionally demonstrated that scan geometry modifies the directional sensitivity of the reconstructed turbulence components. In the investigated configuration, increasing beam separation shifted the reconstruction sensitivity away from the eastward velocity component and toward the northward component.

The LES case study provided further evidence that the deviations introduced by non-collocated reconstruction are not merely random reconstruction artifacts, but contain physically meaningful information associated with spatial variability of the atmospheric flow. While the non-collocated reconstruction underestimates the spatial variability of wind speed compared to LES, it reproduces the spatial variability of turbulence intensity comparatively well. This suggests that the reconstruction behaves partly as a spatial smoothing operator for the mean flow while still retaining relevant turbulence variability relevant for offshore wind applications. Furthermore, the temporal variability derived from the non-collocated reconstruction remained consistent with both the collocated reconstruction and the in-situ cup measurements, indicating that the method preserves the dominant temporal turbulence dynamics.

Overall, the results suggest that non-collocated DSL reconstruction can provide representative turbulence measurements and physically meaningful information on spatial flow variability over kilometer-scale domains. This opens new possibilities for offshore wind resource characterization, specially spatial turbulence assessment using relatively sparse scanning lidar configurations.

Data availability. The wave buoy data are publicly available through the Coastal Monitoring Program at https://coastalmonitoring.org/. The scanning lidar and large-eddy simulation datasets can be obtained from the corresponding owner upon request. The meteorological mast data were provided under an agreement with Offshore Renewable Energy Catapult (OREC) and are therefore subject to third-party restrictions. Requests for access to these data should be directed to OREC.

Appendix A

To establish a baseline error for Phase 2, the sampling frequency of the SL_N system was reduced to match the lower sampling rate associated with the Phase 2 scan configuration. Figure A1 shows the impact of sampling rate on the DSL reconstruction.

https://doi.org/10.5194/wes-2026-99
Preprint. Discussion started: 15 July 2026

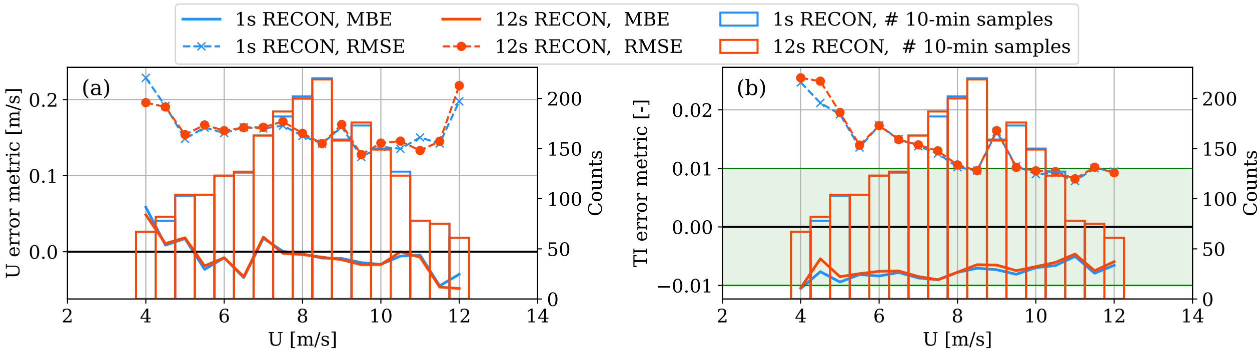

Figure A1. The impact of sampling rate on the SL_N-SL_S reconstruction error for wind speed (a) and TI (b). The orange markers depicts the reconstruction error when selecting LOS data from SL_N system every 12 s. Here only bins with more than 50 samples are shown.

705 **Appendix B**

The timeseries of reconstructed wind speed and TI are compared with LES in Figure B1. The time between 05-08-2026 12:00 and 06-08-2026 08:00 is removed from the simulated dataset due to turbulence not being well developed in the LES.

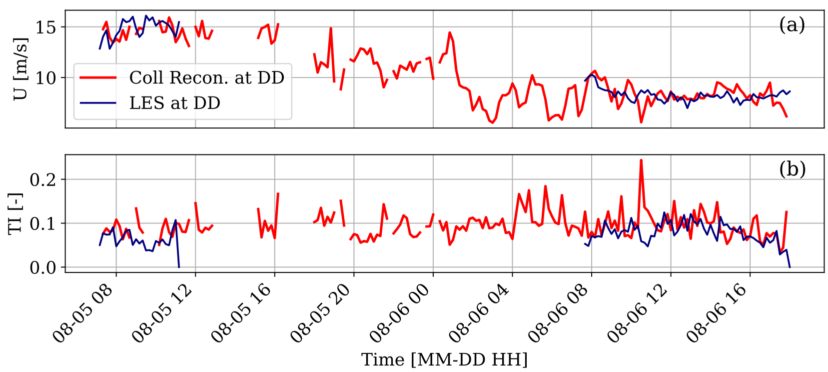

Figure B1. Wind speed (a) and TI (b) timeseries during the LES case study period.

The spatial fields of wind speed, direction and TI given by the non-collocated reconstruction are depicted in Figure B2 (a-c) at a given timestamp. These fields can be compared against the LES fields shown in panels (d-f). The mean and standard

710 deviation of the presented fields are shown above each panel.

https://doi.org/10.5194/wes-2026-99
Preprint. Discussion started: 15 July 2026

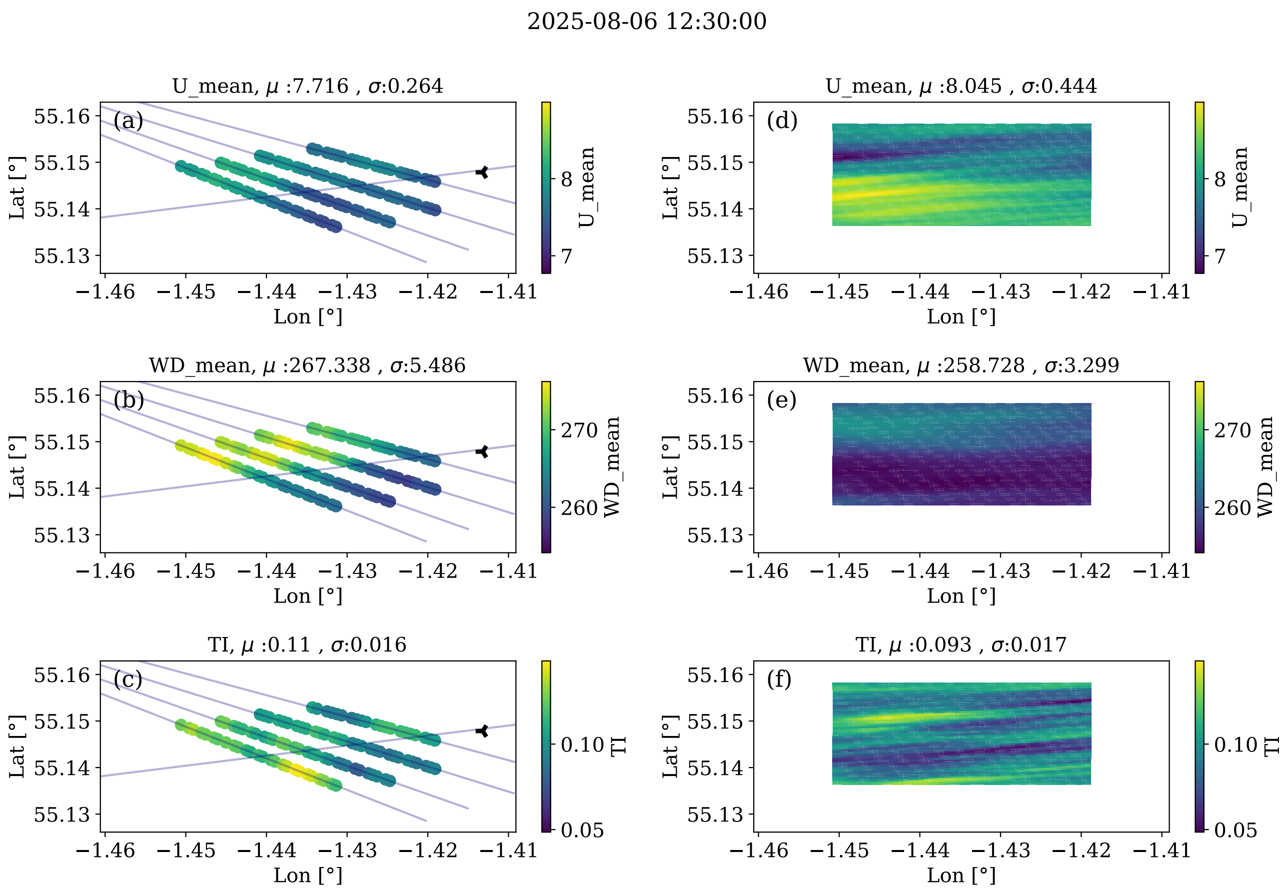

Figure B2. 10-min wind speed (upper panels), wind direction (middle panels) and TI (lower panels) from the non-collocated reconstruction (a-c) and LES (d-f). μ and σ above each panel denote the spatial mean and standard deviation of the samples at the shown timestamp.

Author contributions. FHR and JG conceptualized, designed, and implemented the measurement campaign. TL performed the large-eddy simulations. FHR processed the measurement data, developed the reconstruction framework, and conducted the cross-comparison and sensitivity analyses. JG and TL contributed to the interpretation of the results through extensive discussions. FHR wrote the original manuscript draft, and JG and TL critically reviewed and revised the manuscript.

Competing interests. One of the (co-)authors is a member of the editorial board of Wind Energy Science.

https://doi.org/10.5194/wes-2026-99
Preprint. Discussion started: 15 July 2026

Acknowledgements. This work was conducted as part of the R&D project NEMO – New Methods for Turbulence Measurements and Models in Offshore Wind, funded through the ICON program of the Fraunhofer-Gesellschaft and led by Fraunhofer IWES. Additional support was provided by France Énergies Marines and the French Government through the DRACCAR-NEMO project (ANR-10-IEED-0006-34, PI: Maxime Thiébaut). The authors thank Didier Ricard and Maxime Thiébaut for valuable discussions on the LES setup and for supporting Farkhondeh Rouholahnejad's research stay at CNRM, which facilitated the collaboration underlying this work. We gratefully acknowledge Oldbaum Services for their support on the measurement campaign, particularly Andy Oldroy, Matthew Young, and Matthew Docherty. We thank Offshore Renewable Energy Catapult (OREC) for providing the meteorological mast data, Thies Johnsen for processing the wave buoy data and calculating the bulk Richardson number, and the Northeast Regional Coastal Monitoring Programme for making the wave buoy observations available. ChatGPT was used to improve sentence structure and readability of the manuscript.

https://doi.org/10.5194/wes-2026-99
Preprint. Discussion started: 15 July 2026

References

Ahmadi-Baloutaki, M. and Aliabadi, A. A.: A Very Large Eddy Simulation Model Using a Reductionist Inlet Turbulence Generator and Wall Modeling for Stable Atmospheric Boundary Layers, Fluid Dynamics, 56, 413–432, https://doi.org/10.1134/S0015462821020026, 2021.

Archer, C. L.: Brief communication: A note on the variance of wind speed and turbulence intensity, Wind Energy Science, 10, 1433–1438, https://doi.org/10.5194/wes-10-1433-2025, 2025.

Beck, H. and Kühn, M.: Dynamic Data Filtering of Long-Range Doppler LiDAR Wind Speed Measurements, Remote Sensing, 9, https://doi.org/10.3390/rs9060561, 2017.

Berg, J., Vasiljevíc, N., Kelly, M., Lea, G., and Courtney, M.: Addressing Spatial Variability of Surface-Layer Wind with Long-Range WindScanners, Journal of Atmospheric and Oceanic Technology, 32, 518 – 527, https://doi.org/10.1175/JTECH-D-14-00123.1, 2015.

Brossier, C. L., Ducrocq, V., and Giordani, H.: Two-way one-dimensional high-resolution air–sea coupled modelling applied to Mediterranean heavy rain events, Quarterly Journal of the Royal Meteorological Society, 135, 187–204, https://doi.org/10.1002/qj.338, 2009.

Carbon Trust: Remote Wind Measurements Offshore Using Scanning LiDAR Systems, Technical report, Carbon Trust Offshore Wind Accelerator (OWA), London, United Kingdom, https://www.carbontrust.com/sites/default/files/documents/resource/public/owa-scanning-lidar-final-report-public-version.pdf, 202.

Carbon Trust: Offshore Wind Accelerator roadmap for the commercial acceptance of floating lidar technology (Version 3.0), https://www.carbontrust.com/sites/default/files/2025-09/Updated%2003.09%20OWA%20W%20UFLR%20Updated%20FLS%20roadmap_2025_V3.pdf, 2025.

Channel Coastal Observatory: Quality Assurance and Quality Control of Waves Data Manual, National Network of Regional Coastal Monitoring Programmes, version 1.2 edn., https://coastalmonitoring.org/ccoresources/dataqualitycontrol/WavesQCManual_v1.2.pdf, 2024.

Charnock, H.: Wind Stress on a Water Surface, Quaterly Journal Royal of the Meteorological Society, 1955.

Cheynet, E., Jakobsen, J. B., Snæbjörnsson, J., Mann, J., Courtney, M., Lea, G., and Svardal, B.: Measurements of Surface-Layer Turbulence in a Wide Norwegian Fjord Using Synchronized Long-Range Doppler Wind Lidars, Remote Sensing, 9, https://doi.org/10.3390/rs9100977, 2017.

Cuxart, J., Bougeault, P., and Redelsperger, J.-L.: A turbulence scheme allowing for mesoscale and large-eddy simulations, Quaterly Journal Royal of the Meteorological Society, 126, 1–30, https://doi.org/10.1256/qj.03.130, 2000.

Fairall, C. W., Bradley, E. F., Hare, J. E., Grachev, A. A., and Edson, J. B.: Bulk Parameterization of Air–Sea Fluxes: Updates and Verification for the COARE Algorithm, Journal of Climate, 16, 571–591, https://doi.org/10.1175/1520-0442(2003)016<0571:BPOASF>2.0.CO;2, 2003.

Floors, R., Peña, A., Lea, G., Vasiljevic, N., Simon, E., and Courtney, M.: The RUNE Experiment–A Database of Remote-Sensing Observations of Near-Shore Winds, https://doi.org/10.20944/preprints201610.0070.v1, 2016.

Frehlich, R.: Effects of Wind Turbulence on Coherent Doppler Lidar Performance, Journal of Atmospheric and Oceanic Technology, 14, 54–75, https://api.semanticscholar.org/CorpusID:123507553, 1997.

Fuertes, F. C., Iungo, G. V., and Porté-Agel, F.: 3D Turbulence Measurements Using Three Synchronous Wind Lidars: Validation against Sonic Anemometry, Journal of Atmospheric and Oceanic Technology, 31, 1549 – 1556, https://doi.org/10.1175/JTECH-D-13-00206.1, 2014.

Gottschall, J., Courtney, M. S., Wagner, R., Jørgensen, H. E., and Antoniou, I.: Lidar profilers in the context of wind energy–a verification procedure for traceable measurements, Wind Energy, 15, 147–159, https://doi.org/https://doi.org/10.1002/we.518, 2012.

https://doi.org/10.5194/wes-2026-99
Preprint. Discussion started: 15 July 2026

Gottschall, J., Gribben, B., Stein, D., and Würth, I.: Floating lidar as an advanced offshore wind speed measurement technique: current technology status and gap analysis in regard to full maturity, WIREs Energy and Environment, 6, e250, https://doi.org/https://doi.org/10.1002/wene.250, 2017.

Honnert, R., Masson, V., Lac, C., and Nagel, T.: A Theoretical Analysis of Mixing Length for Atmospheric Models From Micro to Large Scales, Frontiers in Earth Science, 8, https://doi.org/10.3389/feart.2020.582056, 2021.

IEC 61400-1: IEC 61400-1: Wind energy generation systems – Part 1: Design requirements, https://webstore.iec.ch/en/publication/26423, 2019.

Kaimal, J. C. and Finnigan, J. J.: Atmospheric Boundary Layer Flows: Their Structure and Measurement, Oxford University Press, New York, ISBN 9780195062397, https://doi.org/10.1093/oso/9780195062397.001.0001, 1994.

Kelberlau, F. and Mann, J.: Cross-contamination effect on turbulence spectra from Doppler beam swinging wind lidar, Wind Energy Science, 5, 519–541, https://doi.org/10.5194/wes-5-519-2020, 2020.

Kelberlau, F., Neshaug, V., and Venu, A.: Assessment of turbulence intensity estimates from floating lidar systems, Journal of Physics: Conference Series, 2507, 012 014, https://doi.org/10.1088/1742-6596/2507/1/012014, 2023.

Lac, C., Chaboureau, J. P., Masson, V., Pinty, J. P., Tulet, P., Escobar, J., Leriche, M., Barthe, C., Aouizerats, B., Augros, C., Aumond, P., Auguste, F., Bechtold, P., Berthet, S., Bielli, S., Bosseur, F., Caumont, O., Cohard, J. M., Colin, J., Couvreux, F., Cuxart, J., Delautier, G., Dauhut, T., Ducrocq, V., Filippi, J. B., Gazen, D., Geoffroy, O., Gheusi, F., Honnert, R., Lafore, J. P., Brossier, C. L., Libois, Q., Lunet, T., Mari, C., Maric, T., Mascart, P., Mogé, M., Molinié, G., Nuissier, O., Pantillon, F., Peyrillé, P., Pergaud, J., Perraud, E., Pianezze, J., Redelsperger, J. L., Ricard, D., Richard, E., Riette, S., Rodier, Q., Schoetter, R., Seyfried, L., Stein, J., Suhre, K., Taufour, M., Thouron, O., Turner, S., Verrelle, A., Vié, B., Visentin, F., Vionnet, V., and Wautelet, P.: Overview of the Meso-NH model version 5.4 and its applications, Geoscientific Model Development, 11, 1929–1969, https://doi.org/10.5194/gmd-11-1929-2018, 2018.

Mann, J., Cariou, J.-P. C., Parmentier, R. M., Wagner, R., Lindelöw, P., Sjöholm, M., and Enevoldsen, K.: Comparison of 3D turbulence measurements using three staring wind lidars and a sonic anemometer, Meteorologische Zeitschrift, 18, 135–140, https://doi.org/10.1127/0941-2948/2009/0370, 2009.

Masson, V., Le Moigne, P., Martin, E., Faroux, S., Alias, A., Alkama, R., Belamari, S., Barbu, A., and Boone, A.: The SURFEXv7.2 land and ocean surface platform for coupled or offline simulation of earth surface variables and fluxes, Geoscientific Model Development, pp. 929–960, https://doi.org/10.5194/gmd-6-929-2013, 2013.

National Network of Regional Coastal Monitoring Programmes: Realtime Wave Data Downloads, https://coastalmonitoring.org/realtimedata/?chart=110&tab=download&disp_option=1, accessed 2026-05-11, 2026.

Newman, J. F., Klein, P. M., Wharton, S., Sathe, A., Bonin, T. A., Chilson, P. B., and Muschinski, A.: Evaluation of three lidar scanning strategies for turbulence measurements, Atmospheric Measurement Techniques, 9, 1993–2013, https://doi.org/10.5194/amt-9-1993-2016, 2016.

Newsom, R. K., Berg, L. K., Shaw, W. J., and Fischer, M. L.: Turbine-scale wind field measurements using dual-Doppler lidar, Wind Energy, 18, 219–235, https://doi.org/https://doi.org/10.1002/we.1691, 2015.

Pauscher, L., Vasiljevic, N., Callies, D., Lea, G., Mann, J., Klaas, T., Hieronimus, J., Gottschall, J., Schwesig, A., Kühn, M., and Courtney, M.: An Inter-Comparison Study of Multi- and DBS Lidar Measurements in Complex Terrain, Remote Sensing, 8, https://doi.org/10.3390/rs8090782, 2016.

Peña, A. and Mann, J.: Turbulence Measurements with Dual-Doppler Scanning Lidars, Remote Sensing, 11, https://doi.org/10.3390/rs11202444, 2019.

https://doi.org/10.5194/wes-2026-99
Preprint. Discussion started: 15 July 2026

WIND ENERGY SCIENCE DISCUSSIONS

Pope, S. B.: Turbulent Flows, chap. 3, Cambridge University Press, Cambridge, ISBN 9780521598866, 2000.

Ricard, D., Lac, C., Riette, S., Legrand, R., and Mary, A.: Kinetic energy spectra characteristics of two convection-permitting limited-area models AROME and meso-NH, Quarterly Journal of the Royal Meteorological Society, 139, 1327–1341, https://doi.org/10.1002/qj.2025, 2013.

Sathe, A., Mann, J., Gottschall, J., and Courtney, M. S.: Can Wind Lidars Measure Turbulence?, Journal of Atmospheric and Oceanic Technology, 28, 853 – 868, https://doi.org/10.1175/JTECH-D-10-05004.1, 2011.

Shimada, S., Kogaki, T., Konagaya, M., Mito, T., Araki, R., Ueda, Y., and Ohsawa, T.: Validation of near-shore wind measurements using a dual scanning light detection and ranging system, Wind Energy, 25, 1555–1572, https://doi.org/https://doi.org/10.1002/we.2757, 2022.

Shimada, S., Kogaki, T., Konagaya, M., Mito, T., Misaki, T., Hamada, K., Araki, R., Ohhata, S., Ueda, Y., and Ohsawa, T.: Mutsu 2020 Scanning LiDAR Experiment: Comparison of Dual and Single Scanning LiDAR Systems for Near-Shore Wind Measurement, Wind Energy, 28, https://doi.org/10.1002/we.70003, 2025.

St. Pé, A., Weyer, E., Campbell, I., Arntsen, A. E., Kondabala, N., Mibus, M., Coulombe-Pontbriand, P., Black, A. H., Parker, Z., Swytink-Binnema, N., Jolin, N., Goudeau, B. T., Meklenborg Miltersen Slot, R., Svenningsen, L., Lee, J. C. Y., Debnath, M., Wylie, S., Apgar, D., Fric, T., Michaud, D., Smith, E., Mazoyer, P., Tocco, M., Guillemin, F., Teoh, K., and Meyers, M.: CFARS Site Suitability Initiative: An Open Source Approach to Evaluate the Performance of Remote Sensing Device (RSD) Turbulence Intensity Measurements and Accelerate Industry Adoption of RSDs for Turbine Suitability Assessment, Tech. rep., Zenodo, https://doi.org/10.5281/zenodo.5529750, 2021.

Stull, R.: Errata, pp. 175–180, Springer Netherlands, Dordrecht, ISBN 978-94-009-3027-8, https://doi.org/10.1007/978-94-009-3027-8_15, 1988.

Watson, W., Wolken-Möhlmann, G., and Gottschall, J.: Evaluating the impact of motion compensation on turbulence intensity measurements from continuous-wave and pulsed floating lidars, Wind Energy Science, 10, 2791–2820, https://doi.org/10.5194/wes-10-2791-2025, 2025.

Young, M., Docherty, M., Hung, L.-Y., Oldroyd, A., and Gottschall, J.: How accurate is the beam position of scanning lidars? An intercomparison, Wind Energy Science Discussions, 2026, 1–37, https://doi.org/10.5194/wes-2026-94, 2026.